



저작자표시-비영리-변경금지 2.0 대한민국

이용자는 아래의 조건을 따르는 경우에 한하여 자유롭게

- 이 저작물을 복제, 배포, 전송, 전시, 공연 및 방송할 수 있습니다.

다음과 같은 조건을 따라야 합니다:



저작자표시. 귀하는 원저작자를 표시하여야 합니다.



비영리. 귀하는 이 저작물을 영리 목적으로 이용할 수 없습니다.



변경금지. 귀하는 이 저작물을 개작, 변형 또는 가공할 수 없습니다.

- 귀하는, 이 저작물의 재이용이나 배포의 경우, 이 저작물에 적용된 이용허락조건을 명확하게 나타내어야 합니다.
- 저작권자로부터 별도의 허가를 받으면 이러한 조건들은 적용되지 않습니다.

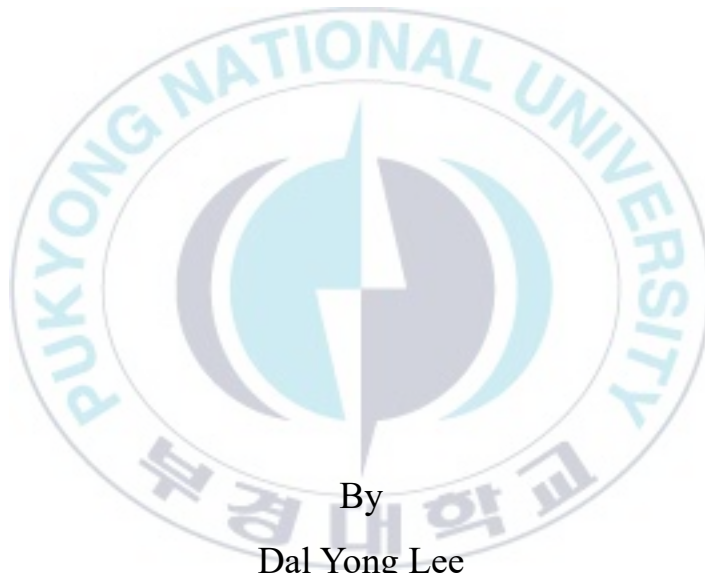
저작권법에 따른 이용자의 권리는 위의 내용에 의하여 영향을 받지 않습니다.

이것은 [이용허락규약\(Legal Code\)](#)을 이해하기 쉽게 요약한 것입니다.

[Disclaimer](#)

Thesis for Degree of Doctor of Philosophy

Efficient Opto-Electronic Materials and Devices
for Printable Light-Emitting Display



By

Dal Yong Lee

Department of Physics

The Graduate School

Pukyong National University

February 2020

Efficient Opto-Electronic Materials and Devices for Printable Light-Emitting Display

(인쇄형 디스플레이를 위한 고효율 광전자 소재
및 소자에 관한 연구)

Advisor: Prof. Sung Heum Park

By
Dal Yong Lee

A Thesis submitted in partial fulfillment of the requirements
for the degree of

Doctor of Philosophy

In Department of Physics, The Graduate School,
Pukyong National University

February 2020

Efficient Opto-Electronic Materials and Devices
for Printable Light-Emitting Display

A dissertation
by
Dal Yong Lee

Approved by:



Prof. Jung Hyun Jeong
Chairman, Ph. D.



Prof. Semo Son
Member, Ph. D.



Prof. Woon Ik Park
Member, Ph. D.



Prof. Bo Ram Lee
Member, Ph. D.



Prof. Sung Heum Park
Member, Ph. D.

February 2020

CONTENTS

ABSTRACT	IX
CHAPTER 1 MOTIVATION	1
1.1 PEROVSKITE LIGHT-EMITTING DIODES (PELEDs)	1
1.2 ORGANIC FIELD-EFFECT TRANSISTORS (OFETs)	3
CHAPTER 2 THEORY	4
2.1 PEROVSKITE LIGHT-EMITTING DIODES	4
2.1.1 <i>Perovskite crystal structure</i>	4
2.1.2 <i>Optical and electronic properties of perovskite</i>	5
2.1.3 <i>Perovskite light-emitting diodes</i>	6
2.1.4 <i>PeLED operating principles</i>	9

2.1.5	<i>PeLED characterization</i>	11
2.2	ORGANIC FIELD-EFFECT TRANSISTORS (OFETs)	12
2.2.1	<i>OFET device structure</i>	12
2.2.2	<i>OFET operating principle</i>	14
2.2.3	<i>Drain current characterization</i>	16
	REFERENCES	17
CHAPTER 3	EXPERIMENTAL METHODS	20
3.1	PEROVSKITE LIGHT-EMITTING DIODES	20
3.1.1	<i>Device Fabrications</i>	20
3.1.2	<i>Device Characterization</i>	20
3.2	ORGANIC FIELD-EFFECT TRANSISTORS	21
3.2.1	<i>Device Fabrications</i>	21
3.2.2	<i>Device characterizations</i>	22

3.3	FILM MORPHOLOGY CHARACTERIZATION	22
3.4	J-V-L EQUIPMENT SETUP	22

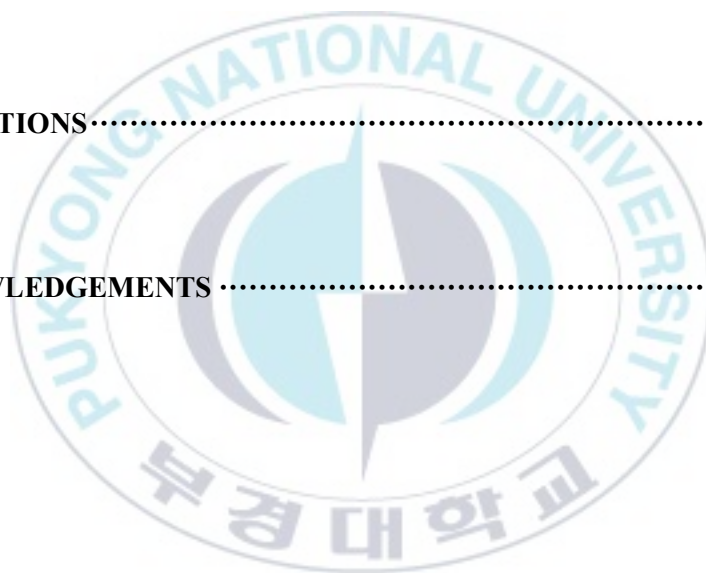
CHAPTER 4 OPTICAL AND PHYSICAL PROPERTIES OF NANO-POLYCRYSTALLINE CSPBBR3 THIN-FILM WITH OLIGOELECTROLYTE PASSIVATION..... 26

4.1	INTRODUCTION.....	26
4.2	RESULT AND DISCUSSION	30
4.3	CONCLUSION	46
	REFERENCES.....	47

CHAPTER 5 SOLUTION-PROCESSABLE AMBIPOLAR ORGANIC FIELD-EFFECT TRANSISTORS WITH BILAYER TRANSPORT CHANNELS 50

5.1	INTRODUCTION.....	50
-----	-------------------	----

5.2	RESULT AND DISCUSSION	53
5.3	CONCLUSION	64
	REFERENCES	65
	CHAPTER 6 SUMMARY AND OUTLOOK.....	69
	PUBLICATIONS.....	70
	ACKNOWLEDGEMENTS	76



LIST OF FIGURES

FIGURE 2.1 PEROVSKITE CRYSTAL STRUCTURE	5
FIGURE 2.2 DEVICE STRUCTURE OF PEROVSKITE LIGHT-EMITTING DIODES	8
FIGURE 2.3 ENERGY DIAGRAM SCHEME FOR PeLED.....	10
FIGURE 2.4 DEVICE STRUCTURES OF (A) BOTTOM GATE BOTTOM CONTACT, (B) BOTTOM GATE TOP CONTACT, (C) TOP GATE BOTTOM CONTACT, AND (D) TOP GATE TOP CONTACT OFETs	13
FIGURE 2.5 OFET STRUCTURE WITH SCHEME OF THE TRANSPORT CHANNEL (A) IN LINEAR ID REGIME AND (B) IN PINCHED-OFF REGIME.	15
FIGURE 4.1 PHOTOLUMINESCENCE (PL) PROPERTIES OF CsPbBr ₃ PEROVSKITE FILMS WITH OLIGOELECTROLYTE PASSIVATION. (A) INTEGRATED PL, AND (B) NORMALIZED PL SPECTRA OF THE FILMS. (C) PL IMAGES OF THE CsPbBr ₃ WITHOUT AND WITH OLIGOELECTROLYTE.	32
FIGURE 4.2 OPTICAL DENSITY AND U _{BARCH} ENERGY OF THE PC-CsPbBr ₃ @COE	

THIN-FILM. (A) OPTICAL DENSITY OF THE CsPbBr₃ FILMS WITH OLIGOELECTROLYTE PASSIVATION. CROSS-SECTIONAL SEM IMAGE OF THE CsPbBr₃ FILMS (B) WITHOUT, AND (C) WITH 20% OLIGOELECTROLYTE. (D) DERIVATION OF THE LOGARITIC ABSORBANCE (LOG A) AT NEAR OF THE BANDGAP RANGE AND (E) EXTRACTED URBACH ENERGY AS FUNCTION OF OLIGOELECTROLYTE FRACTION..... 33

FIGURE 4.3 SURFACE MORPHOLOGY OF PC-CSPbBr₃ THIN FILM OF (A) PURE CsPbBr₃ FILM (B) P6 PASSIVATED CSPbBr₃ FILM, AND (C) P6 PASSIVATED CSPbBr₃ WITH POLYETHYLENE GLYCOL (PEG). (D) THE HISTOGRAM 38

FIGURE 4.4 CRYSTALLOGRAPHIC ANALYSIS OF THE CSPbBr₃ FILMS (A) X-RAY DIFFRACTION (XRD) PATTERNS OF THE CSPbBr₃ FILMS. FRACTIONAL BAR PLOTS OF CRYSTAL ORIENTATION (C) WITH THE RATIO OF (101) AND (202), AND (D) WHOLE ASSIGNED PEAKS ON THE XRD. 39

FIGURE 4.5 DEVICE STRUCTURE AND PERFORMANCE OF CsPbBr₃ PELEDs. (A) CROSS-SECTIONAL SCANNING ELECTRON MICROSCOPY (SEM) IMAGE AND THE DEVICE STRUCTURE OF THE PELED. (B) J-V-L CHARACTERISTICS AND (C) CURRENT EFFICIENCY WITH RESPECT TO J OF THE PELEDs..... 42

FIGURE 4.6 WORK FUNCTION TUNABILITY OF THE P6 PASSIVATOR AND ITS DERIVATIVES. EFFECTIVE WORK FUNCTIONS OF THE SURFACE OF (A) THE PEROVSKITE LAYER IN PELED AND (B) THE OLIGOELECTROLYTES ON THE ITO SUBSTRATES..... 43

FIGURE 4.7 P6 PASSIVATED PELED PERFORMANCES WITH THE ADJUSTMENT OF THE WORK FUNCTION OF HTL. (A) THE DEVICE STRUCTURE, (B) CURRENT EFFICIENCY, (C) ENERGY DIAGRAM, AND (D) J-V-L CHARACTERISTICS OF THE PELED WITH WORK FUNCTION MODIFIER. 44

FIGURE 5.1. (A) MOLECULAR STRUCTURE OF PBDTTPPD AND PCBM IN THE BILAYER. (B) ABSORBANCE VARIATION OF PBDTTPPD (BLACK SQUARES) AND PCBM (RED CIRCLES) DISSOLVED IN DCM WITH INCREASING MOLECULAR CONCENTRATION FOR MONOCHROMATIC INCIDENT LIGHT. (C) SPECTRAL ABSORBANCE SPECTRA OF PCBM (BLACK), PBDTTPPD/PCBM BILAYER (RED), PRISTINE PBDTTPPD (BLUE), AND THE DIFFERENCE IN ABSORBANCE BETWEEN PCBM AND THE PBDTTPPD/PCBM BILAYER (GREEN). (D) AVERAGED THICKNESS (1 MM WIDTH ALONG SCANNING DIRECTION) SURFACE PROFILE OF THE PBDTTPPD AND PCBM FILMS MEASURED BY THE ATOMIC FORCE MICROSCOPY (INSET)..... 55

FIGURE 5.2. (A) STRUCTURE OF THE AMBIPOLAR ORGANIC FIELD-EFFECT TRANSISTOR AND ITS CROSS-SECTIONAL TRANSMISSION ELECTRON MICROSCOPY (TEM) IMAGE. ENERGY DIAGRAMS OF THE DEVICE UNDER THE FOLLOWING OPERATING CONDITIONS: (B) N-TYPE TRANSISTOR AND (C) P-TYPE TRANSISTOR MODES. 57

FIGURE 5.3. OUTPUT CHARACTERISTIC CURVES (A, B) AND TRANSFER CHARACTERISTIC CURVES (C, D) OF THE DEVICE IN EACH OPERATING MODE: P-TYPE (A, C) AND N-TYPE (B, D). BLUE LINES IN (C, D) SHOW THE SQUARE ROOT OF THE DRAIN CURRENT CURVES. 59

FIGURE 5.4. (A) DEVICE STRUCTURE OF THE BILAYER FET TREATED BY THE DIO ADDITIVE. (B) ELECTRON MOBILITY AND (C) HOLE MOBILITY OF THE DEVICE WITH AND WITHOUT THE DIO TREATMENT (WITH INCREASING PBDTTPPD THICKNESS). (D) BALANCED MOBILITY OF THE ELECTRONS AND HOLES WITH AND WITHOUT THE DIO TREATMENT. 62

Abstract

인쇄형 디스플레이를 위한 고효율 광전자

소재 및 소자에 관한 연구

이 달 용

부 경 대 학 교 물 리 학 과

요 약

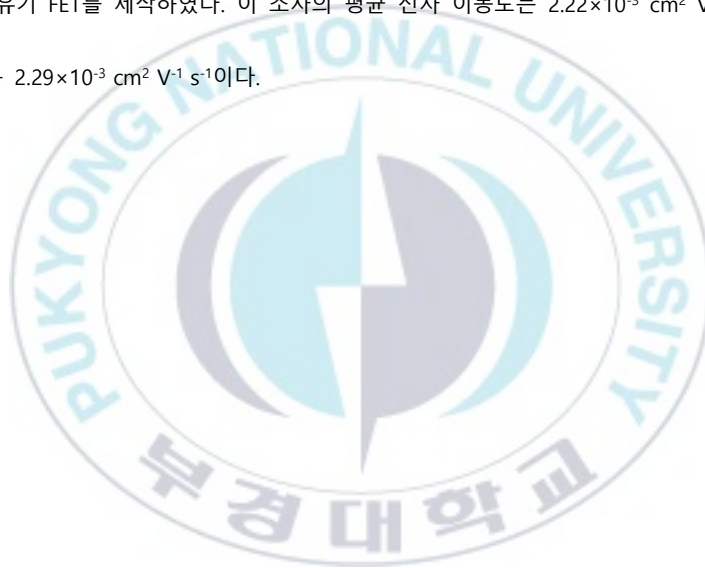
최근 발광 다이오드를 이용한 능동 행렬(active matrix) 구동 방식의 디스플레이는 높은 명암비와 색 재현성, 발광 효율(luminous efficacy), 가벼운 무게 등의 장점으로 주목받고 있다. 대표적으로 현재 상용화되어 있는 유기 발광 다이오드(organic light-emitting diode, OLED)의 점유율은 휴대기기 디스플레이 시장에서 급격하게 증가하며 60%를 넘어섰다. 반면 대형 디스플레이에서는 세도우 마스크(shadow mask)가 처지는 증착 공정 상 문제로 인해, 용액 공정 기술의 필요성이 대두된다. 인쇄형 디스플레이 기술은 대형화 외에도 공정이 단순하면서 생산 속도를 크게 높일 수 있다는 장점이 있다. 용액 공정에 기반한 LED와 장효과 트랜지스터(field-effect transistor, FET)는 인쇄형 디스플레이의

제작을 위한 핵심 기술이다.

LED에 도입이 시도되고 있는 할라이드 페로브스카이트는 높은 색 순도와, 밝기, 고효율을 달성하기 유리하다는 잠재성으로 인해 용액 공정 기반 LED를 위한 유망한 물질로 떠오르고 있다. 그러나 페로브스카이트 LED(perovskite LED, PeLED)의 외부 양자 효율(external quantum efficiency, EQE)이 다른 LED 기술과 격차가 여전히 남아있기 때문에, EQE 격차를 줄이기 위한 다양한 방법들이 제안되고 있다. PeLED의 EQE 손실은 비방사 재결합(nonradiative recombination)을 야기하는 에너지 트랩과 높은 굴절률로 발생하는 전반사에 의한 광-트랩에 크게 연관되어 있다. 본 연구에서는, 페로브스카이트 표면 트랩 제거를 위해 유기 이온을 함유한 신규 공액 올리고전해질(COE)을 패시베이터로 도입하여 페로브스카이트 박막의 형광(photoluminescence)을 크게 증가시켜 PeLED의 효율을 개선하였다. COE 패시베이션을 통해 무기 페로브스카이트 다결정성 박막의 Urbach tail 에너지가 30.6 eV까지 감소하였다. 또한 COE는 기존의 암모늄 기반 패시베이터와 같이 박막의 수명을 크게 증가시켰고, 또한 기존 고분자 전해질과 같이 유효 일함수를 변화시키는 특성을 보였다. COE는 페로브스카이트 보완하는 다기능성 패시베이터로서 기존 패시베이터 사이의 부조화 효과를 해결함으로써, 차기 연구에 중요한 방향을 제시해 줄 것이다.

전자 이동도와 정공 이동도가 균형을 이루는 양극성(ambipolar) 장효과 트랜지스터(FET)는 빠른 반응속도와 낮은 잡음을 갖는 고성능 유기 상보성 회로를 구현하는 데 매우 중요하다. 본 연구에서 우리는 여태껏 구현되지 못했던 다른 활성층 구조를 갖는 양극성 FET 소자를 구현하였다. 특히 양극성 FET의 활성층에 이중층 구조를 성공적으로 도입하였으며, 활성층 물질로 기존 전자 주개 단위체인 benzodithiophene (BDTT)와 새로운 전자 받개 단위체인 2,5-dioctyl-4,6-di(thiophen-2-

yl)pyrrolo[3,4-c]pyrrole-1,3(2H,5H)-dione(PPD)로 이루어진 신고분자 물질을 정공 수송 물질로 이용하고 [6,6]-penyl-C₆₁-butyric-acid-methyl-ester(PCBM)을 전자 수송 물질로 이용하였다. n⁺⁺ Si/ SiO₂ 기판 위에 서로 다른 용해도를 갖는 용매를 이용하여 PBDTTPD/ PCBM를 이중층 구조로 제작한 후, 그 위에 소스/ 드레인 전극으로 Au를 증착하였다. 제작된 FET에서는 n 타입 동작과 p 타입 동작이 모두 관측되었으며, 알려진 것과 같은 양극성 전류 특성 곡선이 나타났다. 또한 PBDTTPD 박막의 두께 조절을 통해 두 타입의 전도도를 쉽게 조절할 수 있었으며, 완전하게 균형이 이루어진 양극성 전도를 보이는 유기 FET를 제작하였다. 이 소자의 평균 전자 이동도는 $2.22 \times 10^{-3} \text{ cm}^2 \text{ V}^{-1} \text{ s}^{-1}$ 이며, 평균 정공 이동도는 $2.29 \times 10^{-3} \text{ cm}^2 \text{ V}^{-1} \text{ s}^{-1}$ 이다.



Chapter 1 Motivation

Since the first development of commercial display in 1930's in the form of television, display technology has evolved rapidly, with the aim of large screens, light weight, high image resolution, and efficient power consumption. Nowadays the display has become an indispensable electronic device as an interface for modern life linking humans with mass media, personal computers processing electronic data, and status information of such manufacturing machines. The most important devices of the state-of-the-art displays are light-emitting diodes (LEDs) that emit the primary colors, and thin-film field-effect transistors (FETs) that control the power of the LEDs.

The general goal of this dissertation is the improvement of the solution-processed devices for printable displays by applying advanced organic materials on fabrication steps.

1.1 Perovskite Light-Emitting Diodes (PeLEDs)

The replacement of early bulky, cathode ray tube (CRT) screen displays with compact, light-weight, energy-efficient alternative technologies such as LCDs, OLEDs, PDPs was a hardware revolution that began with PC monitors in the late 1990s. The OLED displays, especially, have drawn attention by its superior properties,

such as thin, flexible, printable, and light-weight. The organic emissive materials for the active layer in OLED, however, have disadvantages of high materials production cost and complex evaporation process for the fabrication, which increase the unit cost of production. Solution-processed OLEDs, which generally consist of conjugated polymers as an active material, have been demonstrated as an alternative to evaporation-processed OLEDs. Nonetheless, there are still problems such as burn-in and the high cost of organic materials.

Recently, the solution-processed LEDs employ novel emissive materials such as quantum dots and metal halide perovskites to get lower material cost and higher stability. The LEDs based on halide perovskite materials show superior properties such as ultra-pure color, bandgap tunability, and excellent charge carrier mobility. In particular, very low trap concentration of perovskite materials brings the performance of the perovskite solar cells close to the GaAs devices. Despite the outstanding potential of the PeLEDs, the intrinsic weakness of the halide perovskites such as surface traps, short life-time, and incompatibility with conventional organic charge transport layers still remained huddles for the commercialization. In Chapter 4, it is discussed that a new type of passivator, conjugated oligoelectrolytes, improve the performance of the PeLEDs.

1.2 Organic Field-Effect Transistors (OFETs)

Today, virtually all TVs, PC monitors and mobile screens that use LCD or OLED technology employ active matrix technology. In active matrix method of switching individual elements (e.g. LEDs), each pixel is attached to a transistor maintaining the pixel state while other pixels are being addressed. OFETs are gaining much attention due to their potential for low-cost, large-area electronics and flexibility. Compared to conventional FETs, furthermore, OFETs have their own applications such as ambipolar OFETs and light-emitting transistors. The ambipolar OFETs, particularly, is a key component to fabricate organic complementary integrated circuits (ICs) that is a necessary component of disposable electronics such as near field communication (NFC) tag and attachable circuits for internet of things (IoT) technology. In Chapter 5, efficient ambipolar OFETs based on the bilayer architecture of p-type polymer and n-type molecular are discussed.

Chapter 2 Theory

2.1 Perovskite light-emitting diodes

In recent years, metal halide perovskites, which have a general chemical formula of ABX_3 ($A = CH_3NH_3^+$, Cs^+ ; $B = Pb^{2+}$, Sn^{2+} ; $X = Cl^-$, Br^- , I^-), have emerged as a new type of semiconducting materials.[1] Perovskites have lots of advantages, including low cost, tunable structure, tunable band gap, various processing methods, excellent optical properties, and exceptional electrical properties.[2] All of these outstanding properties enabled us to build up highly efficient optoelectronic devices (i.e., solar cells, light-emitting diodes, photodetectors, and optically pumped lasers) based on metal halide perovskites.[3-5]

2.1.1 Perovskite crystal structure

Metal halide perovskites are usually possessed of chemical formula of ABX_3 , in which A stands for small organic or inorganic cations (i.e. $CH_3NH_3^+$, Cs^+), B stands for divalent metal cations (i.e. Pb^{2+} , Sn^{2+}), and X stands for halide anions (i.e. Cl^- , Br^- , I^-). The crystal structure of the ABX_3 type of metal halide perovskites is shown in Figure 2.1. This type of traditional three-dimensional perovskites can be considered as a framework of corner-sharing octahedra (i.e., PbI_6^{4-}) that extends in all three-

dimensional spaces, with small ions, such as CH_3NH_3^+ and Cs^+ , doped in the void spaces between corner-sharing octahedrons.[6]

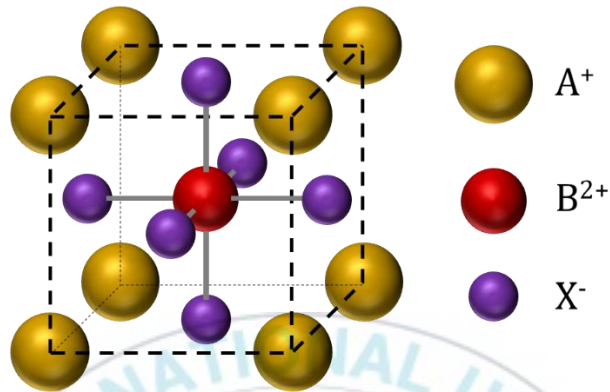


Figure 2.1 Perovskite crystal structure

2.1.2 Optical and electronic properties of perovskite

Perovskites have high absorption coefficient, low exciton binding energy, and high charge carrier mobility. Furthermore, by the extremely low trap density of the perovskite crystal nature, the perovskite has a very narrow photoluminescence spectrum showing high color purity.[7] The bandgap of the perovskite could be modified easily by changing halide components such as chloride, bromide, and iodide in the range from blue to near-IR.[8,9] This superior properties, high color purity and tunable bandgap make the perovskite materials acceptable for the application of light-emitting diode. Many research groups have improved this fly in the ointment of the

halide perovskite materials by various techniques, then the halide perovskite could be made up for defects by the three major categories. First, filling the surface trap sites, which are originated from halide vacancy on the perovskite grains, is essential to reduce nonradiative recombination and degradation from the surface.[3,10] With this halide addition, its counter ions have allowed various functionality to the electrical and chemical properties of the perovskite such as adjusting conducting channels between the perovskite grains, preventing decomposition by ambient air or water, and confining the perovskite grains into 2-dimensional. Another technique is, by introducing a surface modifier below the perovskite, replacing or covering the acidic HTL through various organic EBL to prevent decomposition by acid ions and nonradiative recombination at the interface between HTL/perovskite.[11] The other important enhancement technique for photoluminescence is applying Lewis adducting polymer into the perovskite precursor solution to improve phase stability and light outcoupling by adjusting refractive index of the perovskite thin film.[12] These each technique described above have important role in optoelectronic devices by increasing radiative recombination, crystallinity, film coverage, and phase and environmental stability.

2.1.3 Perovskite light-emitting diodes

Since the first report on a perovskite photovoltaic device using organometallic

perovskite as an active layer, their official efficiency has already exceeded 25% within a decade, owing to improvement of processing techniques, film crystallinity, grain passivation, and phase stabilization.[13] This rapid evolution of perovskite photovoltaics is based on superior optoelectronic properties. In same point of view of the superior properties of the perovskites, it should be able to apply to LED devices. In 2014, Snaith et al. demonstrated highly bright infrared and visible electroluminescence by using three-dimensional perovskites at room temperature for the first time.[14] The infrared light-emitting diodes were based on $\text{CH}_3\text{NH}_3\text{PbI}_x\text{Cl}_{3-x}$ perovskite, while the green emitting LEDs were based on $\text{CH}_3\text{NH}_3\text{PbBr}_3$ perovskite.[15,16] This work clearly demonstrated the potential of metal halide perovskites as emitters for electrically driven LEDs.

(1) Perovskite light-emitting diode structure

In general, the device structure of PeLEDs could be sorted in two types, p-i-n and n-i-p stacks belong to its current flow direction. As shown in Figure 2.2, PEDOT:PSS is frequently employed to HTL owing to its hydrophilic surface properties and high charge carrier transport. For ETL, 2,2',2''-(1,3,5-Benzinetriyl)-tris(1-phenyl-1-H-benzimidazole) (TPBi) layer has shown high performances. A counter electrode is usually aluminum (Al) with LiF doping at the interface ETL/cathode.[16]



Figure 2.2 Device structure of perovskite light-emitting diodes

2.1.4 PeLED operating principles

For generalized p-i-n type LEDs, anode work function matches with valance band of emitting material and cathode work function matches with conduction band of the emitting material.[17] In equilibrium state, which short-circuit with no bias on both electrodes, their work functions were aligned to each other. With forward bias between anode and cathode, the work function of anode get deeper and deeper resulting in the energy distribution becomes flat. After that bias voltage forming flat band, charge carriers start to flow into EmL. After turning on of the PeLED, both charge carriers are struck in EmL and starts forming excitons and recombination. The current increases exponentially along the injection of the charge carriers from the electrodes. When both charge carriers reach to EmL, electron and hole can induce radiative recombination inside the perovskite EmL. So generally, luminescence increases, as current increases. This threshold voltage starting the photons escaping, named as operating voltage.

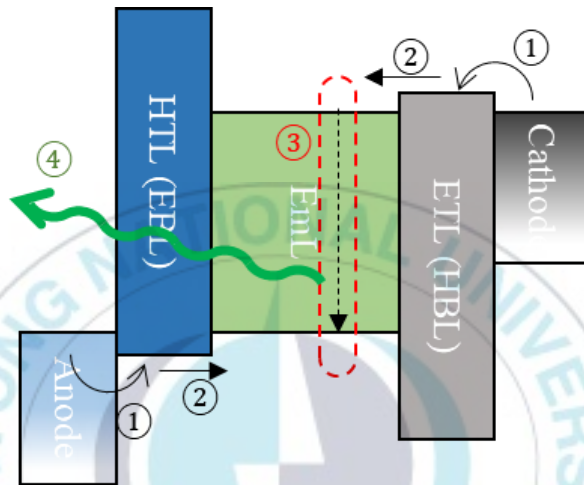


Figure 2.3 Energy diagram scheme for PeLED

2.1.5 PeLED characterization

In general electric characteristics of LEDs are represented by J-V-L curves. As general diode operation under the off-state, PeLED shows Ohmic current flow under the turn-on voltage range. After turning on of the PeLED, current increases exponentially along the injection of the charge carriers from the electrodes. When both charge carriers reach to EmL, electron and hole can induce radiative recombination inside the perovskite EmL. So generally luminescence increases, as current increases. This threshold voltage starting the photons escaping, named as operating voltage. Power conversion efficiency of LEDs, named as wall-plug efficiency, explains how much fraction was converted into optical energy from electric energy. In this case, optical power can be described by the power of electromagnetic energy (radiometry) or the luminance flux by human eyes (photometry). The luminous flux value is preferred for the LEDs with visible colors in the unit of lm W^{-1} . For flat LEDs, current efficiency (or luminance efficacy) is frequently describes how much bright the LED operates in same current. The current efficiency is closely related to other efficiencies, wall-plug efficiency and external quantum efficiency. For last, external quantum efficiency is related to how many charge carriers converted into photons.

2.2 Organic Field-effect transistors (OFETs)

Organic field-effect transistors (OFETs) are essentially identical to inorganic thin-film transistors based on the metal-insulator semiconductor field-effect transistor (MISFET) configuration. The OFETs consist of a organic semiconductor layer and three electrodes called as source, drain, and insulated gate electrode. The drain current I_D flows through the channel at the interface between semiconductor/dielectric. The source electrode injects the charge carriers into the channel and the drain electrode collects the charge carriers. The electric potential of the gate electrode adjust the channel that determines the maximum quantity of current flow. Thus the charge carrier concentration induced by the gate-source voltage (V_{GS}) at the channel plays an important role during the OFET operating.

2.2.1 OFET device structure

The device structure of OFETs is distinguished on the basis of the gate electrode and the contact electrode positions following the MISFET configuration. A schematic illustration of these structures is shown in Figure 2.4. Usually, the OFETs are built as the bottom gate top contact structure due to lower contact resistance at the contact interfaces and simple active material processing. The bottom gate bottom contact structure is also often employed because the structure is easy to mass production by

the lithography techniques.

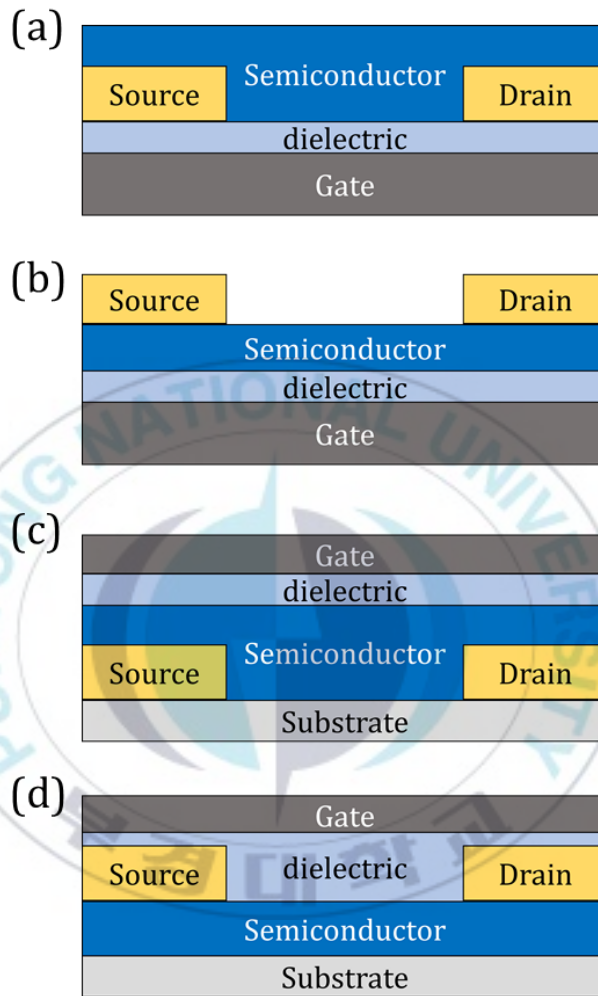
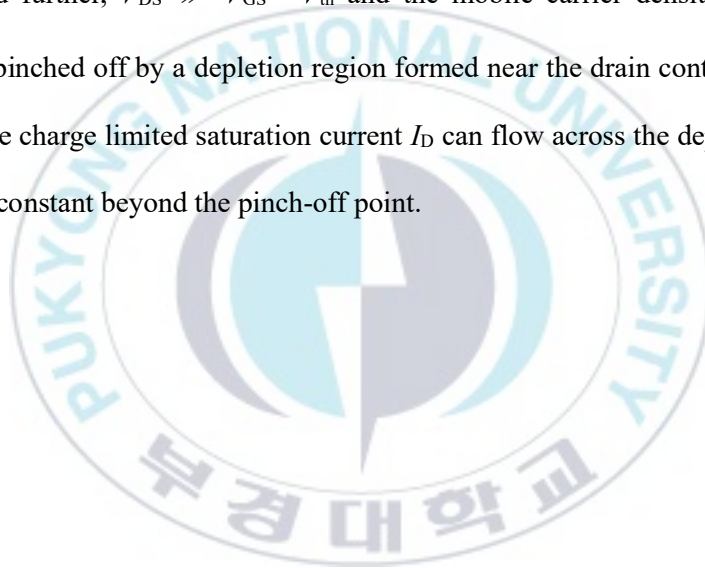


Figure 2.4 Device structures of (a) bottom gate bottom contact, (b) bottom gate top contact, (c) top gate bottom contact, and (d) top gate top contact OFETs

2.2.2 OFET operating principle

The mobile charge carrier given by V_{GS} leads to conductivity in the channel. When a small voltage is applied between the source/drain electrodes, the current start to flowing. When drain-source voltage (V_{DS}) is increased to values approaching V_{GS} , the carrier density is no longer uniform across the channel. As a result, the channel resistance increases and the I_D becomes sublinear with respect to V_{DS} . When the V_{DS} is increased further, $V_{DS} \gg V_{GS} - V_{th}$ and the mobile carrier density within the channel is pinched off by a depletion region formed near the drain contact. Because only a space charge limited saturation current I_D can flow across the depletion zone, I_D remains constant beyond the pinch-off point.



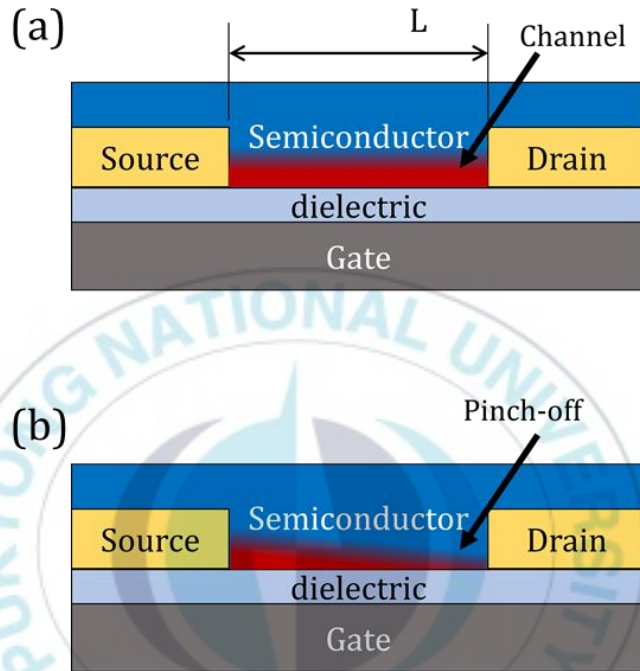


Figure 2.5 OFET structure with scheme of the transport channel (a) in linear ID regime and (b) in pinched-off regime.

2.2.3 Drain current characterization

(1) Linear current region

For small drain-source voltages, $V_{DS} < V_{GS} - V_{th}$, the voltage drop along the channel is homogeneous and I_D equation follows:

$$I_D = \frac{\mu_0 W}{L} \int_0^{V_{DS}} C_i \cdot (V_{GS} - V_{th} - \psi_{DS}(x)) d\psi_{DS} \quad \dots (1)$$

This equation describes the drain current in the linear region.

(2) Current saturation region

When the drain-source voltage is increased and approaches $V_{GS} - V_{th}$, the accumulated charge density underneath the drain contact is more and more reduced by the drain potential. For $V_{DS} = V_{GS} - V_{th}$, the charge density under the drain contact is zero and the conducting channel is pinched-off. A further increase of the drain-source voltage beyond $V_{GS} - V_{th}$ shifts this pinch-off point towards the source contact, causing the drain current to saturate. By replacing V_{DS} with $V_{GS} - V_{th}$ in equation (1), the drain current in the saturation regime is obtained:

$$I_D = \frac{\mu_0 W C_i}{2 \cdot L} \cdot (V_{GS} - V_{th})^2 \quad \dots (2)$$

Generally, the charge carrier mobility could be extracted from the transfer characteristics fitted by the equation (2).

References

- [1] B. R. Sutherland and E. H. Sargent, “Perovskite photonic sources,” *Nat. Photonics*, vol. 10, no. 5, pp. 295–302, 2016.
- [2] L. Li *et al.*, “Self-Filtered Narrowband Perovskite Photodetectors with Ultrafast and Tuned Spectral Response,” *Adv. Opt. Mater.*, vol. 1700672, p. 1700672, 2017.
- [3] M. Abdi-Jalebi *et al.*, “Maximizing and stabilizing luminescence from halide perovskites with potassium passivation,” *Nature*, vol. 555, no. 7697, pp. 497–501, 2018.
- [4] L. Zhao, K. M. Lee, K. Roh, S. U. Z. Khan, and B. P. Rand, “Improved Outcoupling Efficiency and Stability of Perovskite Light-Emitting Diodes using Thin Emitting Layers,” *Adv. Mater.*, vol. 31, no. 2, pp. 1–6, 2019.
- [5] S. A. March *et al.*, “Four-Wave Mixing in Perovskite Photovoltaic Materials Reveals Long Dephasing Times and Weaker Many-Body Interactions than GaAs,” *ACS Photonics*, vol. 4, no. 6, pp. 1515–1521, 2017.
- [6] Q. A. Akkerman *et al.*, “Nearly Monodisperse Insulator Cs₄PbX₆ (X = Cl, Br, I) Nanocrystals, Their Mixed Halide Compositions, and Their Transformation into CsPbX₃ Nanocrystals,” *Nano Lett.*, vol. 6, p. acs.nanolett.6b05262, 2017.

- [7] Y. Wang *et al.*, “Ultrastable, Highly Luminescent Organic–Inorganic Perovskite–Polymer Composite Films,” *Adv. Mater.*, vol. 28, no. 48, pp. 10710–10717, 2016.
- [8] S. Adjokatse, H.-H. Fang, and M. A. Loi, “Broadly tunable metal halide perovskites for solid-state light-emission applications,” *Mater. Today*, vol. 00, no. 00, 2017.
- [9] G. E. Eperon, S. D. Stranks, C. Menelaou, M. B. Johnston, L. M. Herz, and H. J. Snaith, “Formamidinium lead trihalide: a broadly tunable perovskite for efficient planar heterojunction solar cells,” *Energy Environ. Sci.*, vol. 7, no. 3, p. 982, 2014.
- [10] X. Yang *et al.*, “Efficient green light-emitting diodes based on quasi-two-dimensional composition and phase engineered perovskite with surface passivation,” *Nat. Commun.*, vol. 9, no. 1, p. 570, Dec. 2018.
- [11] S. Ahn *et al.*, “Fine Control of Perovskite Crystallization and Reducing Luminescence Quenching Using Self-Doped Polyaniline Hole Injection Layer for Efficient Perovskite Light-Emitting Diodes,” *Adv. Funct. Mater.*, vol. 29, no. 6, pp. 1–10, 2019.
- [12] S. Jeon *et al.*, “Perovskite Light-Emitting Diodes with Improved Outcoupling Using a High-Index Contrast Nanoarray,” *Small*, vol. 1900135, pp. 1–7, 2019.

- [13] H. Shen *et al.*, “Monolithic Perovskite/Si Tandem Solar Cells: Pathways to Over 30% Efficiency,” *Adv. Energy Mater.*, vol. 1902840, p. 1902840, Dec. 2019.
- [14] Z.-K. Tan *et al.*, “Bright light-emitting diodes based on organometal halide perovskite,” *Nat. Nanotechnol.*, vol. 9, no. 9, pp. 687–692, Aug. 2014.
- [15] H. Cho *et al.*, “Overcoming the electroluminescence efficiency limitations of perovskite light-emitting diodes,” *Science (80-.)*, vol. 350, no. 6265, pp. 1222–1225, 2015.
- [16] Y. H. Kim *et al.*, “Multicolored organic/inorganic hybrid perovskite light-emitting diodes,” *Adv. Mater.*, vol. 27, no. 7, pp. 1248–1254, 2015.
- [17] Q. Shan *et al.*, “High Performance Metal Halide Perovskite Light-Emitting Diode: From Material Design to Device Optimization,” *Small*, vol. 13, no. 45, pp. 1–25, 2017.

Chapter 3 Experimental methods

3.1 Perovskite Light-Emitting Diodes

3.1.1 Device Fabrications

The light-emitting diodes were fabricated with a glass/indium tin oxide (ITO)/poly(3,4-ethylenedioxythiophene):poly (styrene sulfonate) (PEDOT:PSS)/perovskite/TPBi/LiF/Al configuration. The glass/ITO substrates were cleaned with water, ethanol, and acetone in an ultrasonic bath for 15 min each, and subsequently treated in a UV-Ozone cleaner for 15 min. Then by first PEDOT:PSS is deposited onto the substrates at 4000 rpm for 40 s and then annealing it at 150 °C for 10 min. After the PEDOT:PSS coating, all preparation steps, and characterization steps were processed in N₂-filled glovebox. The perovskite precursor solution was spin-coated on top of PEDOT:PSS layer at 3000 rpm for 40 s. Then, the substrate was annealed at 70 °C for 5 min. Then, the substrate was transferred into a vacuum chamber. TPBi, LiF, and Al were deposited by thermal evaporation under high vacuum (c.a. 2×10^{-6} Torr) with the thickness 50 nm, 1 nm, 100 nm, respectively. The surface area of Al electrode overlapped with ITO on the glass is 0.135 cm².

3.1.2 Device Characterization

Current density, luminance – bias voltage (JVL) curves were measured with

Keithley 2450 source-multimeter and SpectraWiz BLUE-wave UVIS-50 (StellarNet) spectroradiometer.

3.2 Organic Field-Effect Transistors

3.2.1 Device Fabrications

OFETs were fabricated using a highly n-doped silicon (Si) substrate with a 200 nm layer of thermally grown silicon oxide (SiO₂) as the dielectric. All Si substrates were cleaned by acetone and isopropanol subsequently in an ultrasonic bath and dried in 100 °C to remove any residual solvent. Octadecyltrichlorosilane (OTS) self-assembled monolayer was processed on Si substrate after UV-ozone treatment for 30 min. PBDTTPPD solutions were dissolved in chlorobenzene (CB) with a concentration of 20 mg/ml and stirred for 2 hours at 60 °C. PCBM solutions were dissolved in DCM with a concentration of 20 mg/ml and stirred 30 min at 30 °C. PBDTTPPD layer was deposited on OTS-Si substrate by spin-coating at 800-2000 rpm for 40 sec. And then, PCBM layer was deposited on top of PBDTTPPD layer by spin-coating at 3000 rpm for 10 sec. All solutions were filtered by a 0.45 μm hydrophobic syringe filter before using. Source and drain electrodes were deposited by thermal evaporation using gold with a shadow mask in high vacuum (2.0×10^{-6} Torr). All layer preparation and characterization processes of the OFET were

performed inside N₂-filled globe box.

3.2.2 Device characterizations

Output and transfer characteristics of the OFETs were measured using Keithley 4200 and the mobility was determined using equation (2) with a channel width of 3.00 mm and a channel length of 50.0 μm , and dielectric capacitance of 15 nF cm^{-2} . Characterization processes of the OFET were performed inside N₂-filled globe box.

3.3 Film Morphology Characterization

Atomic force microscopy (AFM) was performed using a Seiko instrument SPI 3800-SPA 400. Transmission electron microscopy (TEM) was performed using JEOL JEM-2100F.

3.4 J-V-L Equipment Setup

LED measurement is designed and manufactured directly to control the measurement conditions flexibly and precisely. The measuring system is built by combining a luminance measuring system with a current-voltage meter. LabVIEW is highly recommended for the design of instruments with simple structures because of their intuitive graphical user interface and ease of debugging through block diagrams.

In addition, LabVIEW has the advantage of high accessibility because the logical computation structure and user interface are separated and the design is very simple. Current-luminance-voltage meters for LED measurement are divided into electrical and optical quantification systems. Current-voltage measurements typically use a source meter, which uses a Keithley 2450 source meter unit as a solution to provide power and measurement of voltage and current. Luminometers include photodiodes, photomultipliers, and sensors using CCDs. Photodiodes have the advantages of simplicity in design, and photodiodes and CCDs have the advantages of high sensitivity and fast response. However, both devices are very difficult to measure by wavelength, making them unsuitable for PeLEDs with easy bandgap control. However, CCD can be combined with diffraction grating in the form of array to construct spectroradiometer to measure the amount of light per wavelength. Therefore, in this study, the spectroradiometer was used to calculate the spectrum and light quantity of LED for PeLED measurement.

One set of JVL information is transmitted to the PC through current measurement with voltage in by the SMU and measurement of the amount of light by wavelength by the SRM. Since the SMU delivers current and voltage in absolute values, it is converted to current density-voltage using the area of the device. On the other hand, the relative value is generally shown from SRM because the spectral signal is largely influenced by the area, structure, and distance of the light source. Therefore, the SRM signal needs to be converted to the spectral radiant flux through calibration in

consideration of the measurement environment according to the measurement structure. In this experiment, the radiant flux were calibrated using the light integration time, the distance from the light source, and the area of the light source.

CCD outputs a certain amount of signal even in the dark due to the heat energy at room temperature. In addition, this signal is mixed with a certain range of noise. It can be assumed that the output signal S is the following equation for the light collection time t , the background light amount φ_0 , and the light source light amount φ for each wavelength.

$$S = S_0 + (\varphi_0 + \varphi)\varepsilon_S t, \quad (1)$$

where S_0 is the dark signal and ε_S is the conversion coefficient. In order to obtain I by removing S_0 and φ_0 , at least one measurement is required for the same t when the light source turned off. Therefore, the amount of background light can be removed from the magnitude of the target signal, and the optical power incident on the SRM can be obtained by dividing by t and the coefficient ε_S .

$$\varphi_{in} = \frac{(S - S(I=0))}{\varepsilon_S t} \quad (2)$$

For a planar LED, the larger the area A of the device and the area A' of the detector, the closer the distance d between the two increases the measured luminous flux. Therefore, the total luminous flux or luminance of the device, which is a measurement amount independent of A , A' , and d , is used.

$$L_{\lambda} = \frac{\varphi_{\lambda}}{\Omega A} \quad (3)$$

In general, however, Ω can be measured under a certain amount of spatial angle Ω_C due to the fixed viewing angle of the SRM. Therefore, the minimum measurable distance is limited by the size of the device. In addition, the luminous flux (light emission degree) E per unit area of the planar light source can be obtained assuming a Lambertian surface.

$$E = \iint_{\text{hemisphere}} L(\theta, \phi) d\Omega \cong \pi L \quad (4)$$

Luminance is obtained by integration for L_{λ} and the luminosity function L .

$$L_V = \int L_{\lambda} L d\lambda \quad (5)$$

The external quantum efficiency η_{EQ} of the LED is calculated through E .

$$\eta_{EQ} = \int \iint \frac{q \cdot L_{\lambda}}{E_0 \cdot J} d\Omega d\lambda \quad (6)$$

Note that when the emission spectrum is close to monochromatic light, such as in PeLEDs, it is possible to approximate as follows.

$$\eta_{EQ} \cong \frac{\pi q \lambda}{h c L} \eta_C \quad (7)$$

In perovskite, the current efficiency value is approximately 4 times EQE in green PeLEDs with an emission peak at 524 nm, 0.5 times at 470nm (Blue), and twice the value at 614nm (Red).

Chapter 4 Optical and Physical Properties of Nano-Polycrystalline CsPbBr₃ Thin-Film with Oligoelectrolyte Passivation

4.1 Introduction

The surpassing optoelectronic properties of halide perovskite have drawn attention by its exceptional characteristics, such as high optical coefficient, bandgap tunability, ultra-color purity, and excellent charge carrier mobility.[1] Since the first report on a perovskite photovoltaic device using organometallic perovskite as an active layer, their official efficiency has already exceeded 25% within a decade, owing to the improvement of processing techniques, film crystallinity, grain passivation, and phase stabilization.[2] The extremely high internal photoluminescence quantum efficiency of perovskite, which rival to those of GaAs, especially, indicates that halide perovskites are optimal materials for optoelectronic devices.[3] Regardless of the rapid advances of perovskite devices, the structural defects, and the chemical, and thermal instabilities of organometallic perovskites are still debating because of their incurable decomposition of organic halide salt components.[4,5] Alternatively, Cs-based inorganic halide perovskite has been applied to recent optoelectronic devices as an active monovalent cation since the compositing and the processing techniques for the inorganic perovskite developed.[6] The inorganic halide perovskite, which is

composed of non-volatile elements, has shown highly increased lifetime and stability in the optoelectronic devices including photovoltaics and light-emitting diodes.[7] The intrinsic shortcomings, which should be treated indispensably, nevertheless, such as grain boundary trap sites by halogen vacancy, decomposition by the moisture in ambient air, and dewetting on the hydrophobic polymer as an electron blocking layer (EBL), still have been obstacles for producing optoelectronic devices.

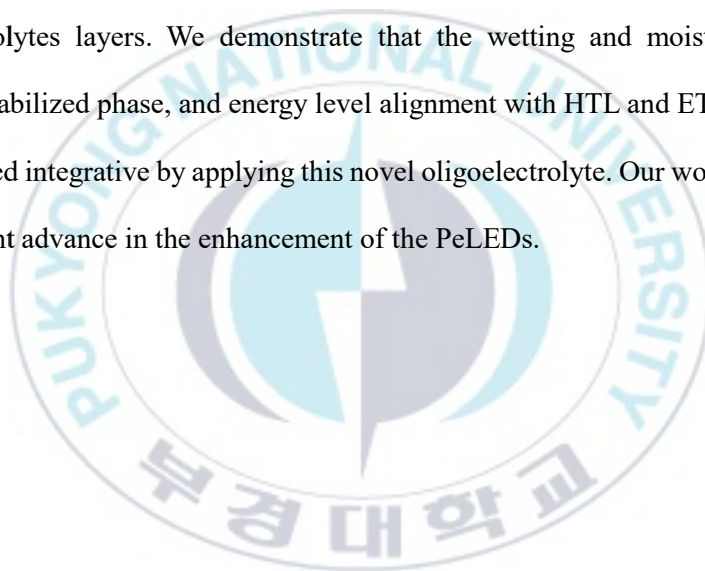
Many research groups have improved these drawbacks of the halide perovskite materials by various techniques, then the halide perovskite could be made up for defects by the three major categories. First, filling the surface trap sites, which are originated from halide vacancy on the perovskite grains, is essential to reduce nonradiative recombination and degradation starting from the grain surface.[3,8] With this halide addition, its counter ions have allowed various functionality to the electrical and chemical properties of the perovskite such as adjusting conducting channels between the perovskite grains, preventing decomposition by ambient air or water, and confining the perovskite grains into 2-dimensional. Another technique is, by introducing a surface modifier below the perovskite, replacing or covering the acidic HTL through various organic EBL to prevent decomposition by acid ions and nonradiative recombination at the interface between HTL/perovskite.[9] The other important effective technique for photoluminescence is Lewis adduct formation by incorporating polymer into the perovskite precursor solution to improve phase stability and light outcoupling by adjusting the refractive index of the perovskite thin

film.[10] These techniques described above have an important role in optoelectronic devices by increasing radiative recombination, crystallinity, film coverage, and phase and environmental stability.

Despite the progress abovementioned, the restricted functionality of a kind of molecule limits the complementary improvement of the perovskite optoelectronic devices. The leakage current and nonradiative recombination still needs to be suppressed by filling the pinholes and surface trap passivation, respectively.[11,12] The interface compatibility is also need to be improved with underlying organic layers.[13] No additive material including this these functionality has existed so far due to limitation of the simple structures of conventional small molecules and of the unit molecules of polymers.[14] To achieve widened functionality including halide fill-up, refractive index matching, and wetting compatibility, the base structure of the functional material needs to be larger as like oligomers. Since these reasons described above, we have supposed the novel type material, the oligoelectrolyte, which has a molecular weight between small and polymer, has to be applied into the halide perovskite thin film.

Here, we demonstrate the multifunctional conjugated oligoelectrolytes over the halide perovskite thin films as an additive to achieve the PeLEDs with high brightness and efficiencies. With a pyridinium functionalized side chains, the conjugated oligoelectrolyte (COE) could passivate the perovskite grain effectively via dissolving

with main solvent of the perovskite precursor solution as like organic salts, and control wetting property within the perovskite solution via on the hydrophobic surface. To the best of our knowledge, no studies have been reported yet regarding the multi-functionalized conjugated oligoelectrolyte on the perovskite based optoelectronic devices; the subject is clearly worthy of investigation. We report substantial improvement of the inorganic perovskite thin-film in photoluminescence (PL) by decorating the surfaces and grain boundaries with conjugated oligoelectrolytes layers. We demonstrate that the wetting and moisture-resistant property, stabilized phase, and energy level alignment with HTL and ETL also could be controlled integrative by applying this novel oligoelectrolyte. Our work represents an important advance in the enhancement of the PeLEDs.



4.2 Result and Discussion

In order to passivate the perovskite grain and grain boundary of the film, we introduced the oligoelectrolyte into the perovskite precursor solution by using the similar polarity of the ion chain of the oligoelectrolyte and the perovskite precursors. Though the both ions have been the blended state in the solution and in the mediate state after spin-casting, the oligoelectrolyte forms at the grain boundary of the perovskite crystals by the phase separation between conjugated arenes and ionic crystals after drying and crystallization of the perovskite film. Because solution-processed perovskite crystals are sensitive to composition ratio of the precursor, we denote the perovskite blended samples as its ionic molar fraction x for the A site cation to neglect large molecular weight of the oligoelectrolyte.[15,16] Since a molecule of the oligoelectrolyte has six side chains with bound ions, the amount of the oligoelectrolyte contained in the precursor solution of x concentration corresponds to $1/6$ of x .

Photo-physical properties of Perovskite thin film with oligoelectrolyte

Since the photoluminescence (PL) properties of the active layer greatly affect on the performance of light-emitting diode, we investigated integrated steady-state photoluminescence (PL) and PL spectra with 320 nm ultraviolet (UV) excitation and

the results are shown in Figure 4.1. The integrated PL intensity over the radiance spectra of the inorganic perovskite films is shown in Figure 4.1a with increasing passivator content x . The PL intensity shows a substantial increase 2.7 times higher when 5% addition of oligoelectrolyte, reaching a very high increase PL intensity 33 times higher than without sample when 30%. When the oligoelectrolyte passivator is over than 40%, the perovskite thin film remains transparent after film annealing and there was no PL from the film. The PL increase such as the result shown in Figure 4.1a could be originated two reasons: (i) enhanced PL quantum efficiency by trap passivation of the ions from the oligoelectrolyte passivator, and/or (ii) the UV absorption increase by the thicker film. This exceptional PL increase is addressed to the trap passivation due to there is no increase of the film thickness described below.

With increase of the PL intensity, the peak position of PL spectrum is also slightly blue-shifted as shown in normalized PL spectrum with different amount of the oligoelectrolyte $x=0$ (pure), 0.05, 0.10, 0.20, and 0.30 in Figure 4.1b. These results imply that the CsPbBr_3 crystals developed in the films containing oligoelectrolyte passivator were much smaller than the pure CsPbBr_3 crystals and thus prevent the excitonic reabsorption of the portion of the short wavelength of the PL spectra. For only 5% of passivating additive, spectral width was reduced from 23 nm when CPB to 21 nm when CPB with 5% oligoelectrolyte. At 30% the FWHM became 19 nm, which show high pure color. Furthermore, only 10% oligoelectrolyte incorporation

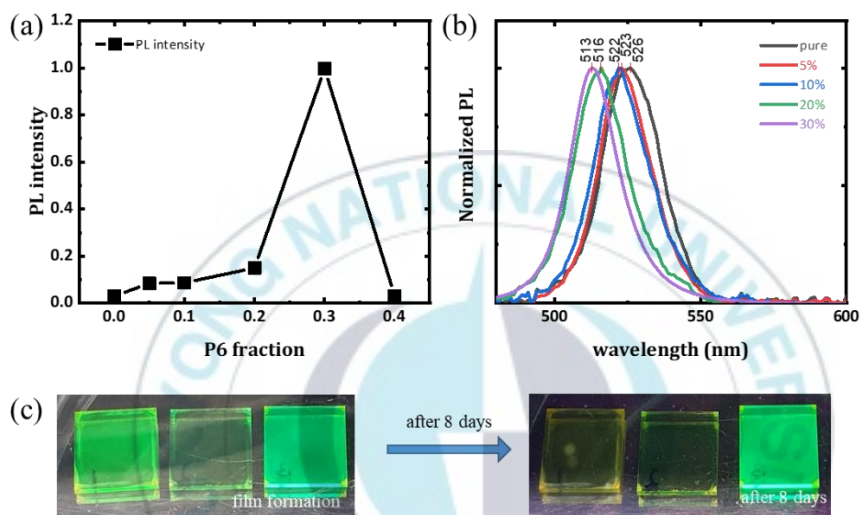


Figure 4.1 Photoluminescence (PL) properties of CsPbBr₃ perovskite films with oligoelectrolyte passivation. (a) Integrated PL, and (b) normalized PL spectra of the films. (c) PL images of the CsPbBr₃ without and with oligoelectrolyte.

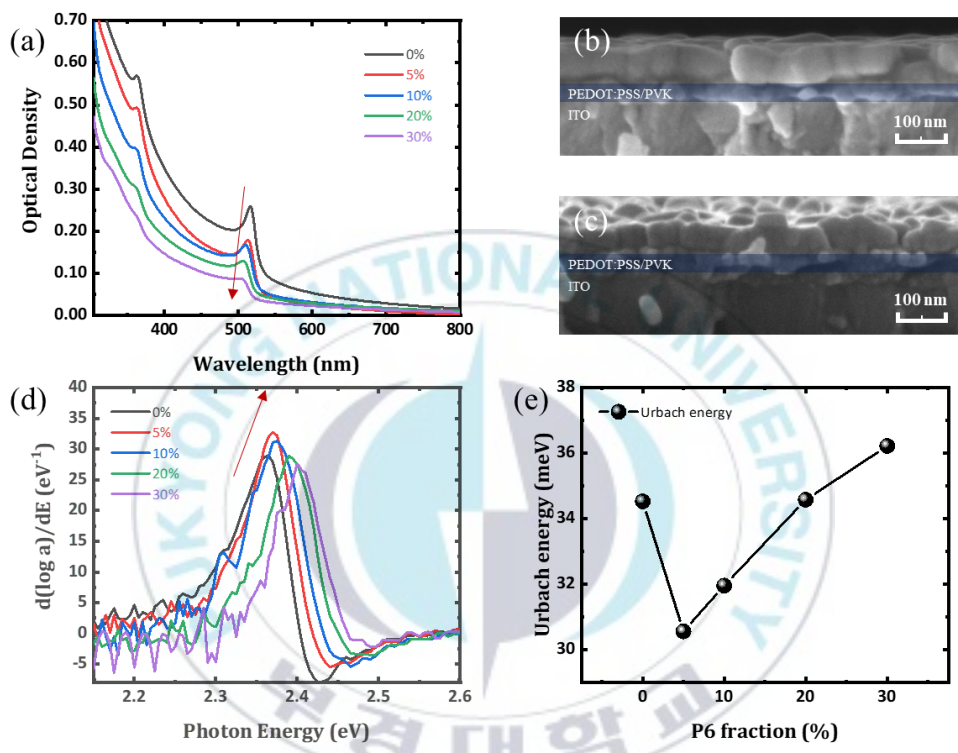


Figure 4.2 Optical density and Urbach Energy of the pc-CsPbBr₃@COE thin-film. (a) Optical Density of the CsPbBr₃ films with oligoelectrolyte passivation. Cross-sectional SEM image of the CsPbBr₃ films (b) without, and (c) with 20% oligoelectrolyte. (d) Derivation of the logarithmic absorbance (log a) at near of the bandgap range and (e) extracted Urbach energy as function of oligoelectrolyte fraction.

prolongs the stability of the CsPbBr₃ crystals after 8 days in ambient air aging whereas PL of pure-CsPbBr₃ became yellow film after aging as shown in Figure 4.1c. The incorporation of PF₆⁻ anions and fluorene conjugated body at the oligoelectrolyte shows that the CsPbBr₃ are passivated at the grain boundary and induced nano-sized crystal successfully.

UV-vis absorbance spectra confirm the formation of nanocrystalline CsPbBr₃ with smooth surface and low reabsorption as shown in Figure 4.2. The absorption edges (Figure 4.2a) for each sample are positioned at each PL peak wavelength. Although whole CsPbBr₃ films with oligoelectrolyte showed highly suppressed absorbance under the bandgap range ($\lambda > 550$ nm), indicating that the surface of the CsPbBr₃ films became low roughness films. The absorbance of continuum states decreases as increase the ratio of oligoelectrolyte because the perovskite density in the CsPbBr₃ film also decreased along with the nano-sized crystallization in the constant film thickness (Figure 4.2b). And sharp excitonic absorption at 512 nm of the pure inorganic perovskite related to crystal size, reduced gradually as more oligoelectrolyte incorporated. In order to observe the reduction of the trap states, Urbach energy was extracted through the derivation of the optical density at the range of the bandgap.[17] The Urbach energy decreased to 30.6 meV from 34.5 meV after incorporation of 10% oligoelectrolyte, showing that CsPbBr₃ grain surface is passivated thorough the ionic interaction by the oligoelectrolyte. We found that the 5 and 10% CsPbBr₃ films show the lowest Urbach energy, and the emission peak

wavelength suddenly jump toward 510 nm over than 20% whereas changes gradually under and over than 20%.

Structural Properties of the perovskite films

The PL enhancement by passivating with oligoelectrolyte can be addressed by structural evolution of the grain morphology of the perovskite thin-film. As shown in Figure 4.3, the pure inorganic perovskite film shows large and non-uniform grains with particularly many pinholes on the film surface. At a 10% blend with oligoelectrolyte addition, the grain size is substantially decreased and fewer small pinholes were observed on Figure 4.3b. With the polyethylene glycol (PEG) blend, pinhole-free perovskite thin-film was formed and became more uniform.

The crystal morphology of perovskite films with and without oligoelectrolyte is analyzed by field-emission scanning electron microscope (FE-SEM), and Figure 4.3 shows the related surface. The surface morphologies of the films with different composition of additives of oligoelectrolyte 0, 10%, and 10% with PEG with respect to mole amount of CsPbBr₃ precursors, were investigated. Apparently, although CsPbBr₃ grains formed almost in large size crystals without oligoelectrolyte, much smaller grains of CsPbBr₃ formed in the presence of oligoelectrolyte 10% with PEG. Notably the small grains developed in the presence of oligoelectrolyte in Figure 4.3b are conserved their crystal phase of 0% CsPbBr₃, as confirmed by PL spectra in which

the intensity of the absorption band at 2.3 eV. No reduction in the grain size was observed in films with additional PEG incorporation; a film with oligoelectrolyte and PEG even prevent crystal growth after film formation in ambient air. The morphology of a film without oligoelectrolyte deposited on either PEDOT:PSS or PVK layer was also examined and the FE-SEM image shows very large grains of the pure-CsPbBr₃ with large intercrystalline voids (Figure 4.3a inset), suggesting the beneficial role of the oligoelectrolyte on the formation of dense and pinhole-free forms with nanocrystalline CsPbBr₃ films in Figure 4.3b inset. We note that the intercrystalline voids named as pinhole cause unavoidably the leakage path, which induce nonradiative recombination of injected charge carriers in the device, by the direct contact between HTL and ETL. Nanocrystalline CsPbBr₃ by the oligoelectrolyte being contrast with pure CsPbBr₃ connote that the ion at the end of the branches bound with the grain surface and suppressed the grain growth.

The passivated perovskite film mainly consists of the perovskite crystals, confirmed by the characteristic X-ray diffraction peaks at 15.2°, 21.6°, 30.6°, and 37.8° corresponding to the (101), (121), (202), and (123) planes, respectively, of the orthorhombic Pnma phase (PDF#54-0752) (Figure 4.4a). The XRD spectrum for CsPbBr₃ shown here is in good agreement with the reference database for the orthorhombic perovskite structure, the notable difference between pure and passivated perovskites being the peak ratio of (110) to (123) plane as shown in Figure 4.4c, d. We note that the (123) peak has increased relative intensity compared to

literature data, suggesting that the processing route used here yield films that are somewhat oriented in the diagonal direction.[18] Because the grain size of passivated perovskite is smaller than that of pure perovskite and the mass fraction of the perovskite is reduced by the portion of passivator, there should be a reflection decline when the perovskite is passivated. Thus, there should also be a corresponding decrease in XRD peaks as the passivator fraction increases. The XRD spectra for $x=0.05$ and 0.10 are thus consistent with the peaks of the pure perovskite that is gradually diminished relative to ITO peak. The identical peak position in XRD spectra from which we can see that those films indicate a same phase and no CsBr residues were observed. By comparing the XRD patterns especially the intensity changes of peaks, we conclude that the oligoelectrolyte passivator induces a directional crystal growth along the (123) facet close to (111) plane, which forms nearly destructive interference with identical crystals to the pure CsPbBr_3 perovskite in nano-metre scale grains.

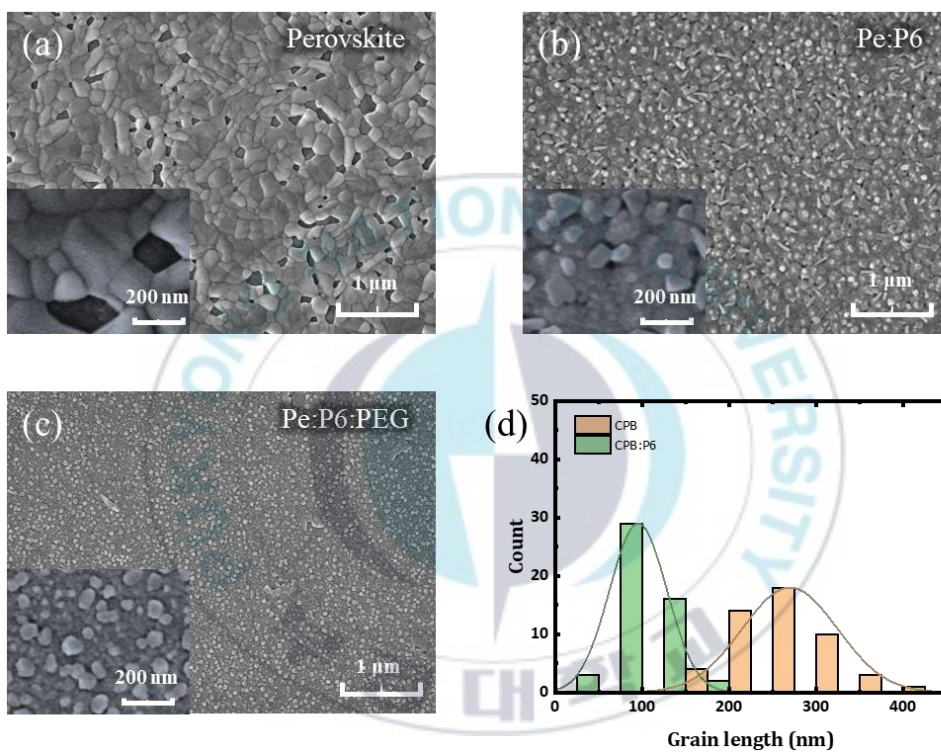


Figure 4.3 Surface morphology of **pc-CsPbBr₃** thin film of (a) pure CsPbBr₃ film (b) P6 passivated CsPbBr₃ film, and (c) P6 passivated CsPbBr₃ with polyethylene glycol (PEG). (d) The histogram

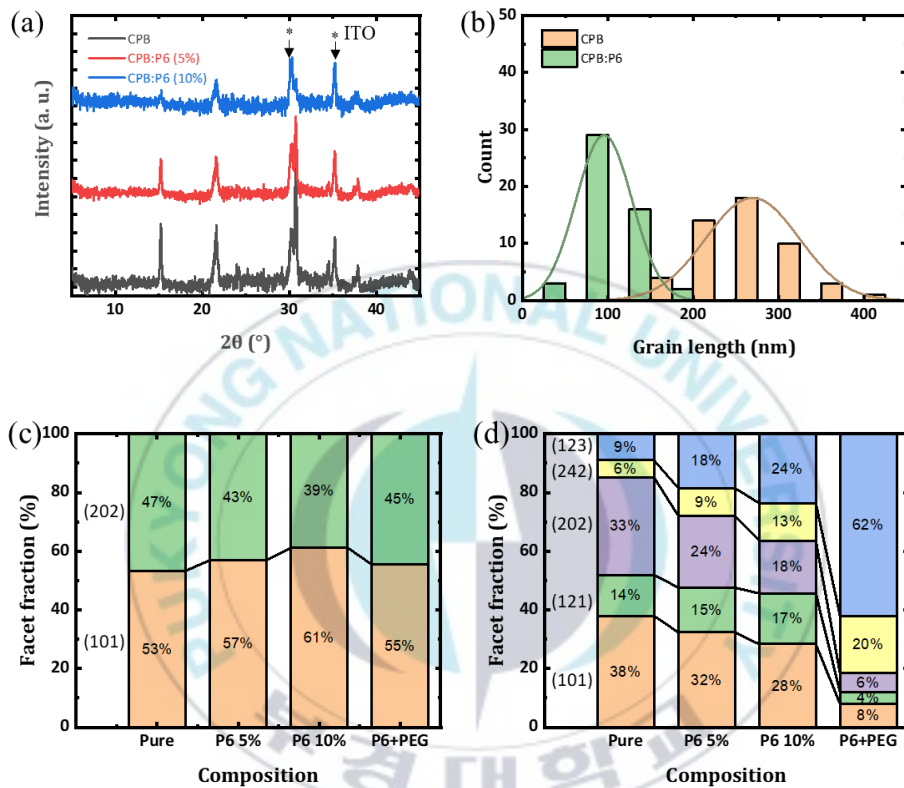


Figure 4.4 Crystallographic analysis of the CsPbBr_3 films (a) X-ray diffraction (XRD) patterns of the CsPbBr_3 films. Fractional bar plots of crystal orientation (c) with the ratio of (101) and (202), and (d) whole assigned peaks on the XRD.

Current-Voltage-Luminance Characteristics of PeLED

Keeping in mind that the 10% composition of oligoelectrolyte CsPbBr₃ film could be a good candidate for an emitting material, we fabricated another batch of devices to verify this hypothesis. We structured the PeLED as ITO/PEDOT:PSS/PVK/CsPbBr₃/TPBi/LiF/Al. PEDOT:PSS is used as a hole injection layer (HIL), PVK as a hole transporting layer (HTL), TPBi as an electron transport layer (ETL), and CsPbBr₃ with oligoelectrolyte as an emission layer (EmL) as shown in Figure 4.5a. The injection current keeps constant from 0% to 30% in Figure 4.5b. Correspondingly, the brightness continue to increase (Figure 4.5b-c), and the 10% oligoelectrolyte based PeLED shows the maximum brightness of about 1000 cdm⁻². We suspect that this might be due to the swallowed effective work function of the CsPbBr₃ over than 20% oligoelectrolyte incorporation due to the passivator has surrounded the CsPbBr₃ crystals with the work function tuning ionic chains (Figure 4.5a). The decreased effective work function with larger molar ratio of oligoelectrolyte can lead to mismatched charge balance in the EmL or charge carrier passing by the EmL, which would have suppressed luminescence of the PeLED.

Although the strong work function rearrangement, we apply bistriflimide (TFSI) anion, which show induce deeper effective work function contrary to the PF⁶⁻, on top of the PVK HTL layer to offset the hinderance of hole injection at the HTL/EmL interface. As shown in Figure 4.7, the operation voltage decreases and the current

density and luminance increases intensely after HTL energy level matching. The best oligoelectrolyte passivated PeLED shows luminance of 12600 cd m^{-2} , which is about 10 times of PF^{6-} only PeLED. Owing to the increasement of the luminance, the CE increase to 2.23 cd A^{-1} , which is about 8 times of PF^{6-} only PeLED.



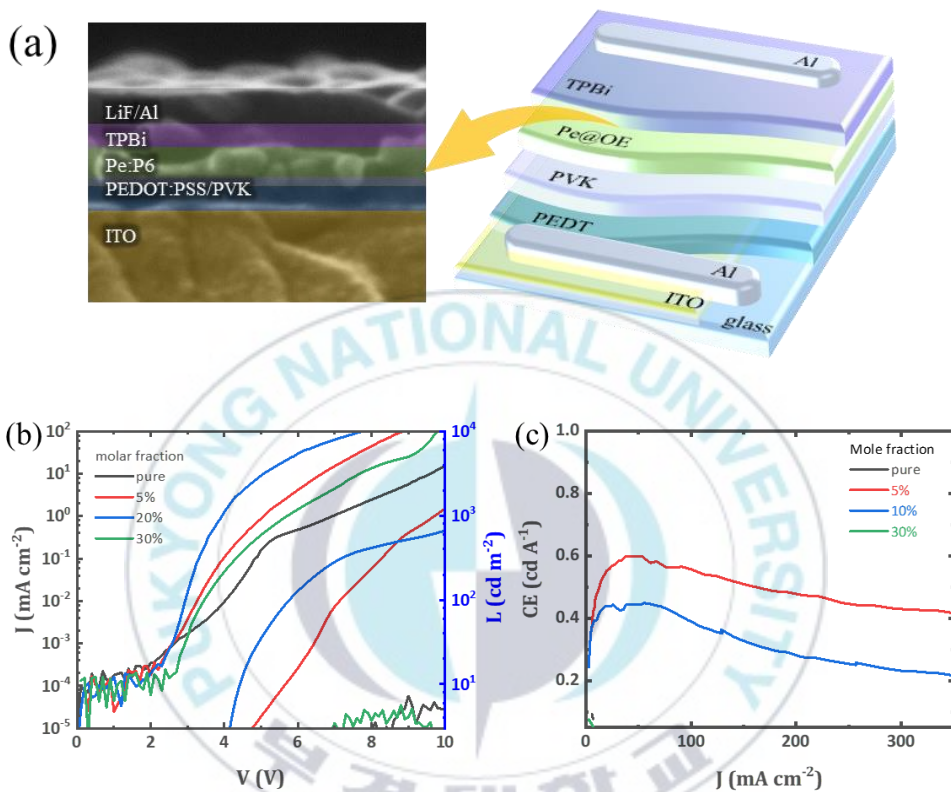


Figure 4.5 Device structure and performance of CsPbBr₃ PeLEDs. (a) Cross-sectional scanning electron microscopy (SEM) image and the device structure of the PeLED. (b) J-V-L characteristics and (c) current efficiency with respect to J of the PeLEDs

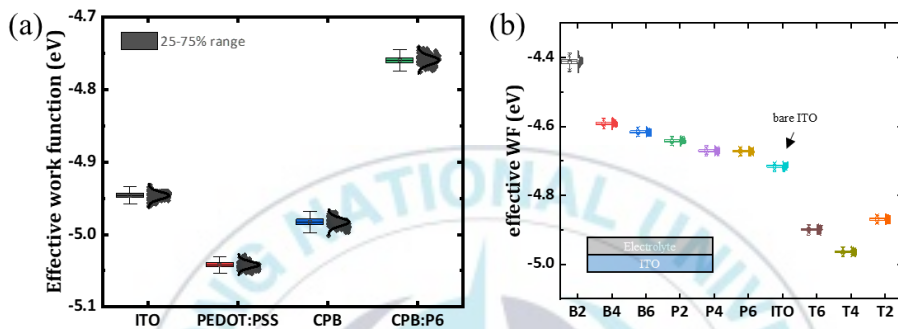


Figure 4.6 Work function tunability of the P6 passivator and its derivatives. Effective work functions of the surface of (a) the perovskite layer in PeLED and (b) the oligoelectrolytes on the ITO substrates.

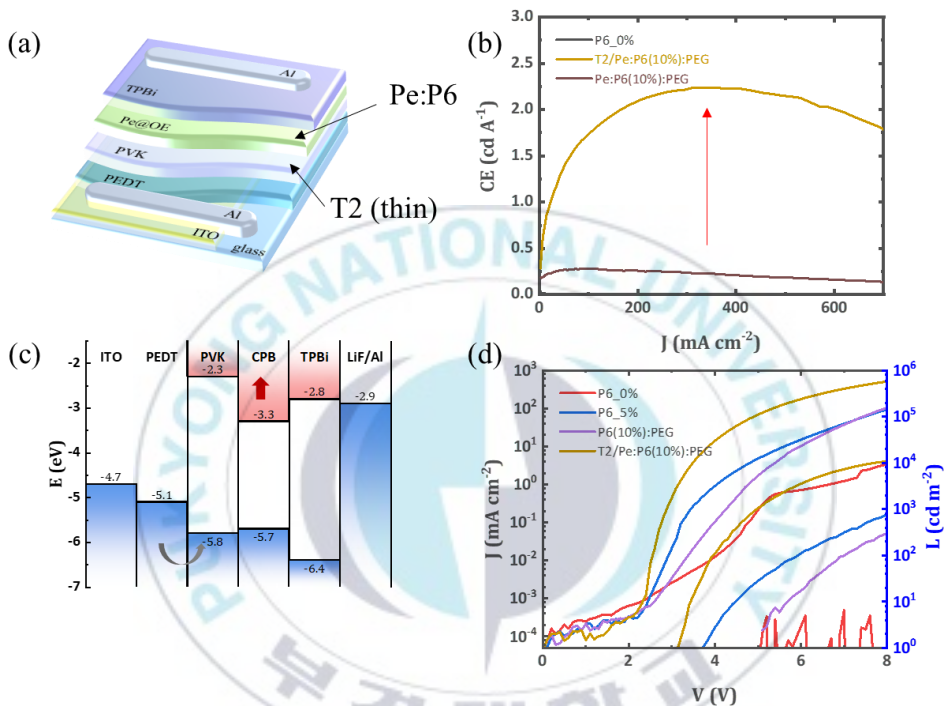


Figure 4.7 P6 passivated PeLED performances with the adjustment of the work function of HTL. (a) The device structure, (b) current efficiency, (c) energy diagram, and (d) J-V-L characteristics of the PeLED with work function modifier.

Table 4.1 Parameters of best-performing PeLEDs

EmL Structure	L_{\max} (cd/m²)	@J (mA/cm²)	Peak (nm)
T2/Pe@P6	12600	720	520
Pe@P6	2030	374	520
Pure Pe	7.25	5.65	524

4.3 Conclusion

We have shown that crystal passivation of CsPbBr₃ with PF₆ branch-type oligoelectrolyte (COE) through the solution-deposition process leads to nanometer-sized crystals, and low Urbach disorder, typical for the long A-site cation introduction. The nanocrystals of the perovskite film have tended to orient its crystal planes when COE introduced into the perovskite film as a GB passivator. Pyridinium functional branches with its counter anion parts (Br⁻, PF₆⁻, and TFSI⁻) on multi-functional conjugated oligoelectrolyte (COE) molecules effectively passivated the grain boundary (GB) of the halide perovskite (or both organic hybrid and inorganic halide perovskite) and enhanced PL intensity (or PL quantum efficiency) from the perovskite thin films after the passivation of the GB. Since COE has much larger bandgap rather than the perovskite emitter, the body of COE, the fluorene, which is located at the GBs through the ion branch interaction, also boosts PL intensity by preventing charge carrier recombination across the GB, (forming multiple quantum well structure) and gives the surface energy compatibility to the perovskite precursor solution on the hole transporting layer (HTL), PVK. Especially, hexafluorophosphate anions, which gives less-hygroscopicity to the COE, enhance the stability of the perovskite thin-film by preventing chemical decomposition induced by the moisture in air. These techniques for the perovskite passivation holds great promise for further high-performance PeLEDs.

References

- [1] Y. Chen *et al.*, “Strain engineering and epitaxial stabilization of halide perovskites,” *Nature*, vol. 577, no. 7789, pp. 209–215, Jan. 2020.
- [2] F. Zhang and K. Zhu, “Additive Engineering for Efficient and Stable Perovskite Solar Cells,” *Adv. Energy Mater.*, vol. 1902579, pp. 1–26, 2019.
- [3] M. Abdi-Jalebi *et al.*, “Maximizing and stabilizing luminescence from halide perovskites with potassium passivation,” *Nature*, vol. 555, no. 7697, pp. 497–501, 2018.
- [4] L. Zhao, K. M. Lee, K. Roh, S. U. Z. Khan, and B. P. Rand, “Improved Outcoupling Efficiency and Stability of Perovskite Light-Emitting Diodes using Thin Emitting Layers,” *Adv. Mater.*, vol. 31, no. 2, pp. 1–6, 2019.
- [5] E. Aydin, M. De Bastiani, and S. De Wolf, “Defect and Contact Passivation for Perovskite Solar Cells,” *Adv. Mater.*, vol. 31, no. 25, p. 1900428, Jun. 2019.
- [6] N. Yantara *et al.*, “Inorganic Halide Perovskites for Efficient Light-Emitting Diodes,” *J. Phys. Chem. Lett.*, vol. 6, no. 21, pp. 4360–4364, Oct. 2015.
- [7] H. Cho, J. S. Kim, Y.-H. Kim, and T.-W. Lee, “Influence of A-site cation on the thermal stability of metal halide perovskite polycrystalline films,” *J. Inf. Disp.*, vol. 19, no. 1, pp. 53–60, 2018.

- [8] X. Yang *et al.*, “Efficient green light-emitting diodes based on quasi-two-dimensional composition and phase engineered perovskite with surface passivation,” *Nat. Commun.*, vol. 9, no. 1, p. 570, Dec. 2018.
- [9] S. Ahn *et al.*, “Fine Control of Perovskite Crystallization and Reducing Luminescence Quenching Using Self-Doped Polyaniline Hole Injection Layer for Efficient Perovskite Light-Emitting Diodes,” *Adv. Funct. Mater.*, vol. 29, no. 6, pp. 1–10, 2019.
- [10] S. Jeon *et al.*, “Perovskite Light-Emitting Diodes with Improved Outcoupling Using a High-Index Contrast Nanoarray,” *Small*, vol. 1900135, pp. 1–7, 2019.
- [11] Y. Ling *et al.*, “Enhanced Optical and Electrical Properties of Polymer-Assisted All-Inorganic Perovskites for Light-Emitting Diodes,” *Adv. Mater.*, vol. 28, no. 40, pp. 8983–8989, 2016.
- [12] S. D. Stranks, V. M. Burlakov, T. Leijtens, J. M. Ball, A. Goriely, and H. J. Snaith, “Recombination Kinetics in Organic-Inorganic Perovskites: Excitons, Free Charge, and Subgap States,” *Phys. Rev. Appl.*, vol. 2, no. 3, p. 034007, 2014.
- [13] A. R. Bin Mohd Yusoff, P. Gao, and M. K. Nazeeruddin, “Recent progress in organohalide lead perovskites for photovoltaic and optoelectronic applications,” *Coord. Chem. Rev.*, 2017.

- [14] J. Peng, Y. Chen, K. Zheng, T. Pullerits, and Z. Liang, "Insights into charge carrier dynamics in organo-metal halide perovskites: From neat films to solar cells," *Chem. Soc. Rev.*, vol. 46, no. 19, pp. 5714–5729, 2017.
- [15] M. H. Park *et al.*, "Efficient Perovskite Light-Emitting Diodes Using Polycrystalline Core–Shell-Mimicked Nanograins," *Adv. Funct. Mater.*, vol. 1902017, p. 1902017, 2019.
- [16] J. Y. Kim *et al.*, "Reversible, Full-Color Luminescence by Post-treatment of Perovskite Nanocrystals," *Joule*, vol. 2, no. 10, pp. 2105–2116, 2018.
- [17] Y. Wu *et al.*, "In Situ Passivation of PbBr₂ Octahedra toward Blue Luminescent CsPbBr₃ Nanoplatelets with Near 100% Absolute Quantum Yield," *ACS Energy Lett.*, vol. 3, no. 9, pp. 2030–2037, 2018.
- [18] M. Zhang *et al.*, "Growth and characterization of all-inorganic lead halide perovskite semiconductor CsPbBr₃ single crystals," *CrystEngComm*, vol. 19, no. 45, pp. 6797–6803, 2017.

Chapter 5 Solution-processable ambipolar organic field-effect transistors with bilayer transport channels

5.1 Introduction

Ambipolar field-effect transistors (A-FETs) which show both n-type and p-type operation functions have drawn considerable attention as a promising element for simply fabricable integrated circuits (ICs).[1–4] Because the A-FET can act as n-type and p-type FETs selectively for low power dissipation and noise squelching in ICs, it leads to significant reduction in the complexity in device fabrication.[5–8] In particular, the ambipolar organic FET (A-OFET) using an organic semiconductor as an active material has additional advantages such as easy fabrication,[9] large processing area,[10] and high flexibility.[11] Moreover, it enables the fabrication of straightforward complementary ICs without any significant change in the device structure of the OFET.[12] Therefore, developing an efficient A-OFET is one of the reasonable approaches to obtain simply processable, highly efficient complementary ICs.

Compared to conventional OFETs with one carrier transport via one carrier channel, the A-OFET can transport both electrons and holes via multi-carrier channels

formed in the active layer of the device.[13] Since the carrier channels formed in the active layer are strongly affected by the configuration of the active layer, fabricating an optimized configuration of the active layer in the A-OFET becomes one of the critical factors in determining the performance of A-OFET devices.[14–16] Two useful methods for the fabrication of an ambipolar active layer for an effective A-OFET have been suggested in previous studies.[17,18] One is the use of organic semiconductors with low bandgap as active materials and two different metals as contact electrodes. In this case, electrons are injected from the lower work-function metal contact, while holes are injected from the higher work-function metal and transported via the active layer. The other is the use of a blend of two organic semiconductors, which show n-type and p-type properties for electron and hole transport, respectively. Both the methods can easily provide efficient A-OFETs; however, both have drawbacks which need to be overcome for commercial applicability. The former method suffers from the limited availability of organic semiconductors with low bandgap as active materials and additional deposition steps are required for the evaporation of a different metal. On the other hand, the use of a blend material as the active layer causes limited charge carrier mobility due to the innumerable junction interfaces in the active layer.

Introducing a bilayer structure with two stacked layers of n- and p-type semiconductors to the device as an active layer is one of the promising approaches to obtain an efficient A-OFET. Because each electron- and hole-carrier moves via a

transport channel formed in one of the bilayers, there are no junctions of the two materials in the lateral direction of charge transport from source to drain electrode. This reduces the trap sites in the active layer due to the straightforward transport channels. Recently, there have been several attempts to construct a separated active layer such as in double-layer OFETs.[19,20] By the deposition of the p-type small molecule and the n-type C60 separately using thermal evaporation, they successfully fabricated a bilayer A-OFET. Although the device works effectively and shows ambipolar properties, the A-OFET is based on small molecules, thus requiring a vacuum process, which has not been matched to the printing technology for mass production. In addition, an effective way to obtain balanced n- and p-type transport characteristics and charge carrier mobility in an A-OFET has not been investigated so far.

In this study, we successfully demonstrate a solution-processable bilayer A-OFET using the semiconducting polymer poly[4,8-bis(5-(2-ethylhexyl)thiophen-2-yl)benzo[1,2-b:4,5-b']dithiophene-alt-2,5-dioctyl-4,6-di(thiophen-2-yl)pyrrolo[3,4-c]pyrrole-1,3(2H,5H)-dione) (PBDTTPPD),[21] and soluble [6,6]-phenyl-C61-butyric acid methyl ester (PCBM). Using the orthogonal solvent dichloromethane (DCM),[22] we repeatedly obtain clear bilayers of the p-type semiconducting polymer PBDTTPPD and n-type PCBM. In addition, the charge carrier mobility of each layer is controlled using additive materials and controlling the PBDTTPPD layer thickness.[23] The A-OFET shows significantly balanced n- and p-type transport

characteristics and charge carrier mobility.

5.2 Result and Discussion

For the effective transport of both electrons and holes in one device, the active layer should consist of n-type and p-type materials. As shown in Figure 1a, typical PCBM and PBDTTPPD are chosen as the components in the active bilayer for electron transport and hole transport, respectively. PCBM is widely used as an electron-transport material in solution-processed thin films, and PBDTTPPD is an acceptable hole-transport material with reasonable hole mobility and has been frequently used as a donor material in recent organic solar cells.[21,24,25] The solution-based bilayer structure of the PBDTTPPD/PCBM is formed by the sequent coating of the two materials dissolved in an organic solvent. Thus, one of the critical problems in the fabrication of the bilayer film is the dissolution of the underlying PBDTTPPD layer by the organic solvent in the PCBM solution.[26,27] Because the PBDTTPPD film dissolves well in common organic solvents such as chlorobenzene (CB), dichlorobenzene (DCB), and chloroform (CF), the use of these solvents in the PCBM solution for the sequent coating leads to the dissolution of the PBDTTPPD layer when the PCBM solution is dropped on the PBDTTPPD layer.[21] To overcome this problem, a solvent that does not dissolve PBDTTPPD but dissolves PCBM is necessary to obtain the complete bilayer structure.

The use of DCM with a strong dipole moment as a solvent for the PCBM solution

enables the realization of the bilayer structure. In fact, the DCM solvent can dissolve both PBDTTPPD and PCBM, and it causes the dissolution of the underlying PBDTTPPD layer when the PCBM solution with DCM is dropped for spin casting. However, we observe that the PBDTTPPD layer hardly dissolves in a PCBM solution with saturated concentration as the molecular weight of PBDTTPPD is higher than that of PCBM. The variation of absorbance versus concentration for the PCBM and PBDTTPPD solutions is shown in Figure 1b. The wavelength of the incident light for absorbance measurement is chosen at 532 nm and 575 nm for PCBM and PBDTTPPD, respectively. As shown in Figure 1b, the absorbances of both the solutions increase linearly with increasing concentration in the washy region. However, the absorbances become constant and saturated when the concentration reaches 0.174 mg/ml for PBDTTPPD and 16.0 mg/ml for PCBM. Therefore, it is expected that PBDTTPPD does not dissolve in a PCBM solution with a concentration higher than 16.0 mg/ml and sinks to the bottom.

Figure 1c shows the absorbance spectra for PCBM film (black line), PCBM/PBDTTPPD bilayer film (red line), PBDTTPPD film (blue line) and the calculated difference in absorbance between the PCBM and bilayer films (green line). As expected, the calculated absorbance matches well with the absorbance of the single PBDTTPPD film; this clearly indicates that the PCBM/PBDTTPPD bilayer is completely formed without any damages to the underlying PBDTTPPD layer. The

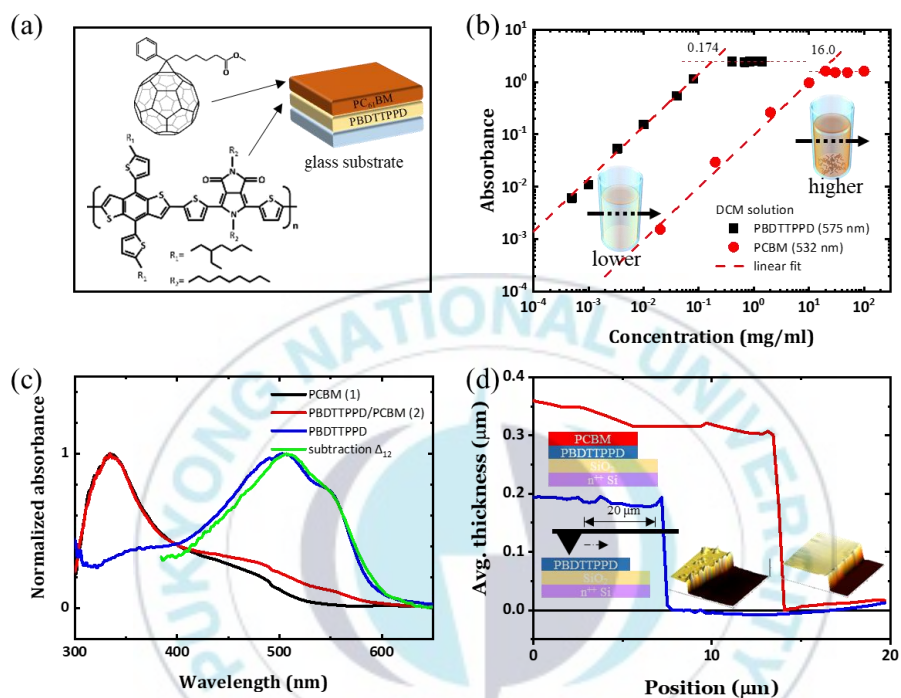


Figure 5.1. (a) Molecular structure of PBDTTPPD and PCBM in the bilayer. (b) Absorbance variation of PBDTTPPD (black squares) and PCBM (red circles) dissolved in DCM with increasing molecular concentration for monochromatic incident light. (c) Spectral absorbance spectra of PCBM (black), PBDTTPPD/PCBM bilayer (red), pristine PBDTTPPD (blue), and the difference in absorbance between PCBM and the PBDTTPPD/PCBM bilayer (green). (d) Averaged thickness (1 μm width along scanning direction) surface profile of the PBDTTPPD and PCBM films measured by the atomic force microscopy (inset).

surface profiles extracted from the atomic force microscopy (AFM) data before and after the deposition of the PCBM layer on the PBDTTPPD film also support our expectation. For the surface profile measurement, we remove the films partially and scan the film surfaces using the AFM. As shown in Figure 1d, the thickness of the single PBDTTPPD film (blue line) is 0.2 μm and that of the PBDTTPPD/PCBM bilayer (red line) is approximately 0.3 μm . Therefore, the thickness of the PCBM film is easily calculated as it is deposited on the PBDTTPPD film and this proves the existence of the complete bilayer of PBDTTPPD/PCBM.

With the complete bilayer on the Si substrate, we fabricate the A-OFET after evaporating Au as the source and drain electrodes on the PBDTTPPD/PCBM bilayer. The final structure of the A-OFET is presented in Figure 2a with a cross-sectional transmission electron microscopy (TEM) image of its active layer. The cross-sectional TEM image shows each layer completely separated and a reasonable thickness of 0.3 μm in the equivalent scale with that measured in the surface profiles in Figure 1d. The conceptual diagrams for the operation of the A-OFET device under n-type and p-type modes are shown in Figures 2b and 2c. The energy levels of highly n-doped Si, PBDTTPPD, and PCBM are drawn relative to each other. In the n-type operation ($\Delta\phi \geq 0$ eV in Figure 2b), the chemical potential (ϕ) is lowered by $\Delta\phi = -qV$ relative to its equilibrium position, tilting the conduction band of the dielectric and bending the conduction band of PBDTTPPD and PCBM at the interface. Since two valleys are formed at the dielectric/PBDTTPPD and the PBDTTPPD/PCBM

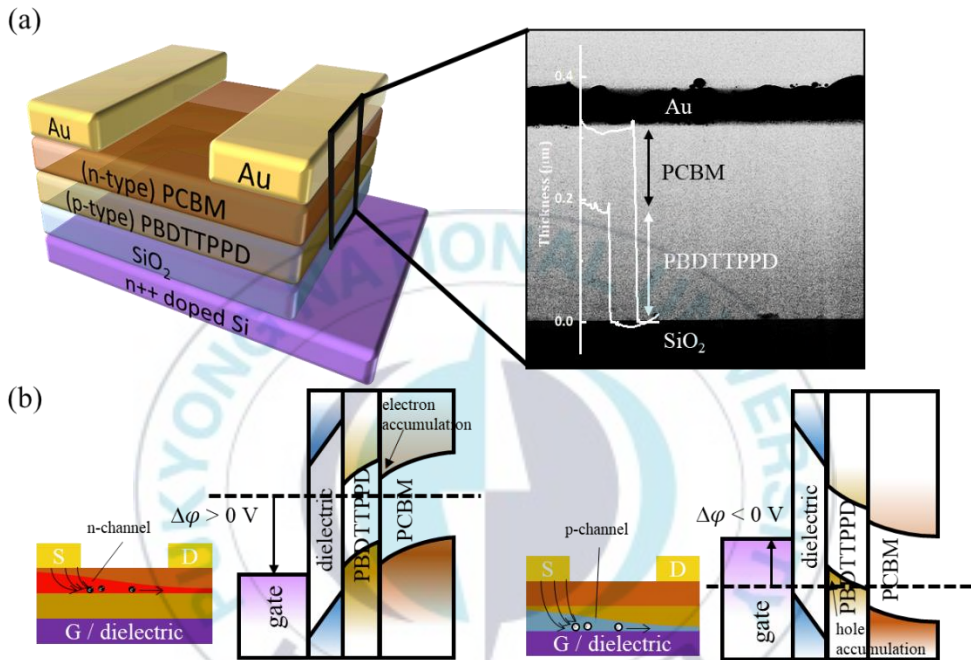


Figure 5.2. (a) Structure of the ambipolar organic field-effect transistor and its cross-sectional transmission electron microscopy (TEM) image. Energy diagrams of the device under the following operating conditions: (b) n-type transistor and (c) p-type transistor modes.

interfaces, the PBDTTPPD/PCBM interface offers the n-type transport channel, whereas the dielectric/PBDTTPPD interface could not transport electrons. Similarly, under p-type operation ($\Delta\phi \leq 0$ eV), the chemical potential of the gate is raised by $-qV$ from its equilibrium position. In this case, only one valley exists below the valance band of PBDTTPPD at the dielectric/PBDTTPPD interface. This valley transports the positive carriers from the source to the drain electrode.

Figures 3a and 3b present the output characteristic curves of drain current versus drain-source voltage for different gate-source voltages (V_{GS}) in the A-OFET under p-type and n-type operation modes, respectively. Due to the minor carrier injection, the A-OFET behaves as a typical diode at low gate-source voltages ($-20V \leq V_{GS} \leq 0$ V). However, the A-OFET device shows unipolar p-type FET characteristics with drain current saturation at high gate-source voltages (-60 V $\leq V_{GS} \leq -30$ V). For n-type channel formation (30 V $\leq V_{GS} \leq 60$ V), the A-OFET device exhibits n-type output characteristics with saturated current, as shown in Figure 3b. This clearly indicates bipolar transport in the A-OFET.

The transfer characteristics of drain current versus gate-source voltage (black curves) of the A-OFET device are shown in Figure 3c for p-type operation (drain-source voltage is -60 V) and in Figure 3d for n-type operation (drain-source voltage is 60 V). As expected, the A-OFET device exhibits clear bipolar transfer characteristics under the fixed drain-source bias conditions of -60 V and 60 V. When

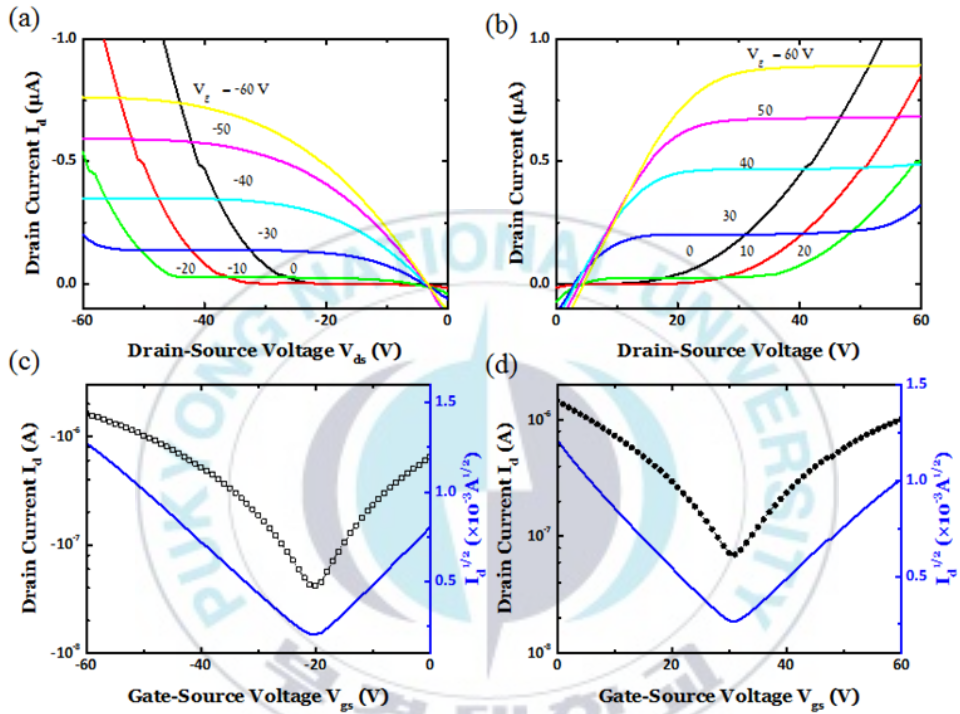


Figure 5.3. Output characteristic curves (a, b) and transfer characteristic curves (c, d) of the device in each operating mode: p-type (a, c) and n-type (b, d). Blue lines in (c, d) show the square root of the drain current curves.

the voltage of -60 V is applied, the device exhibits the minimum values of drain current at the gate-source bias of -20 V. Remarkably, the current gradually increases with not only increasing but also decreasing gate-source voltage. This tendency is also observed when the drain-source voltage of 60 V is applied to the device. The current gradually increases in both directions with the minimum current observed at the gate-source voltage of 30 V (Figure 3d). This confirms that the device operates as an ambipolar transistor and it originates from separated transport channels formed in PBDTTPPD for the holes and in PCBM for the electrons in the bilayer.

The mobilities of the electrons and holes in the A-OFET are extracted from the square root of the drain current (blue) curves in Figures 3c and 3d and the equation (1) below.

$$I_D = \mu_0 \left(\frac{C_{di}W}{2L} \right) (V_{GS} - V_{th})^2 \quad (1)$$

where μ_0 is the field-effect mobility, W and L are the width and the length of the OFET channel, respectively, C_{di} is the capacitance of SiO_2 dielectric, and V_{th} is extracted from the fitted line of the characteristics.

Since the drain current is sensitive to the film thickness and morphology of both the active layers, an optimized condition for higher mobility is obtained by controlling the PBDTTPPD film thickness and the morphology of PBDTTPPD and PCBM.[23] It has been proved that additive solvent treatment is one of the effective

ways to optimize the morphology of active layers in bulk heterojunction polymer solar cells.[28] Adding a small amount of an additive solvent with a high boiling point to the active materials provides a better nanometer-scale morphology of the active layer. As shown in Figure 4a-d, we added the DIO additive to PBDTTPPD and PCBM separately and their combination and monitored the carrier mobilities of the device. In addition, the mobilities are measured for the increasing PBDTTPPD thickness. Figure 4b shows the variation of electron mobility versus increasing PBDTTPPD thickness after adding the DIO additive to PBDTTPPD, PCBM, and their combination. Unexpectedly, the devices treated with DIO show a decrease in the electron mobility compared to the original mobility of $3.83 \times 10^{-3} \text{ cm}^2 \text{ V}^{-1} \text{ s}^{-1}$ on 100 nm thickness of PBDTTPPD layer. Moreover, the electron mobility decreases with increasing PBDTTPPD thickness. However, as shown in Figure 4c, we observe an increase in the hole mobility of the devices treated with the DIO additive. The device in which the DIO additive is added to the combination of the materials shows the highest hole mobility of $7.57 \times 10^{-3} \text{ cm}^2 \text{ V}^{-1} \text{ s}^{-1}$, which is almost two times higher than that of the pristine devices at 100 nm thickness. The hole mobility also slightly decreases with increasing PBDTTPPD thickness.

Compared to the PCBM molecule, the PBDTTPPD has bulk volume and molecular weight. Therefore, it is expected that the morphology change in PBDTTPPD is strongly affected by the addition of the DIO additive compared to PCBM.[29] In addition, since the electric field decreases when the distance between

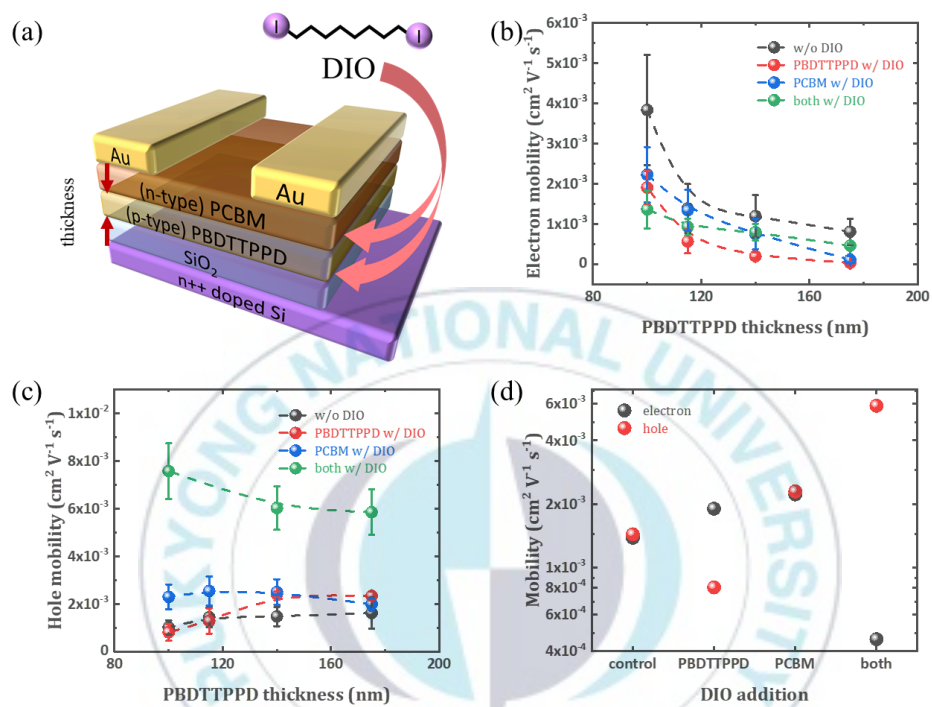


Figure 5.4. (a) Device structure of the bilayer FET treated by the DIO additive. (b) Electron mobility and (c) hole mobility of the device with and without the DIO treatment (with increasing PBDTTPD thickness). (d) Balanced mobility of the electrons and holes with and without the DIO treatment.

the gate electrode and the source electrode increases at a constant gate-source voltage, the decrease in electron and hole mobility with increasing PBDTTPPD thickness is easily understood. Moreover, considering that the electron channel lies at the interface between PBDTTPPD and PCBM, the increasing thickness of PBDTTPPD (which is located between the PCBM layer and the gate electrode) should reduce the electron transport channel width due to the decreased electric field. This electron mobility dependency is probably due to the PBDTTPPD layer playing the role of a dielectric, which varies the effective dielectric capacitance in n-type operation. Finally, balanced carrier mobilities for the A-OFET are obtained with only PCBM treated by DIO. Figure 4d shows the comparison of the carrier mobilities of the device under different DIO-treated conditions. When DIO is added only to PCBM, the device exhibits balanced carrier mobility with an average electron mobility of $2.22 \times 10^{-3} \text{ cm}^2 \text{ V}^{-1} \text{ s}^{-1}$ and an average hole mobility of $2.29 \times 10^{-3} \text{ cm}^2 \text{ V}^{-1} \text{ s}^{-1}$ at 115 nm thickness of the PBDTTPPD film. Therefore, it is obvious that the device operates as an ambipolar transistor.

5.3 Conclusion

In conclusion, we demonstrate a solution-processable A-OFET in this study. By achieving the saturation condition of the DCM solvent for preparing the PCBM solution, we successfully deposited PCBM on PBDTTPPD with no damage. The charge transport channels for the electrons and holes are formed in the PCBM and PBDTTPPD layers of the bilayer, respectively. The A-OFET operates as an n-type and p-type transistor by controlling the gate-source voltage or the drain-source voltage. When a positive bias is applied between the gate electrode and the source electrode, an n-channel for electron transport is generated close to the interface of PCBM and PBDTTPPD, and the device serves as an n-type transistor. On the other hand, a p-channel for hole transport is produced at the interface of PBDTTPPD and SiO₂ dielectric with a negative bias, and the device serves as a p-type transistor. The better-balanced n- and p-type transports are achieved by morphology control using the DIO additive and the PBDTTPPD layer thickness. The optimized device exhibits balanced carrier mobility with an average electron mobility of $2.22 \times 10^{-3} \text{ cm}^2 \text{ V}^{-1} \text{ s}^{-1}$ and an average hole mobility of $2.29 \times 10^{-3} \text{ cm}^2 \text{ V}^{-1} \text{ s}^{-1}$ at 115 nm thickness of the PBDTTPPD film. Because the A-OFET is easily fabricated via the solution process, it presents a potential method for mass production of ambipolar transistor arrays such as roll-to-roll processing.

References

- [1] Z. Ni, H. Wang, H. Dong, Y. Dang, Q. Zhao, X. Zhang, W. Hu, *Nat. Chem.* **2019**, *11*, 271.
- [2] Z. Yi, Y. Jiang, L. Xu, C. Zhong, J. Yang, Q. Wang, J. Xiao, X. Liao, S. Wang, Y. Guo, W. Hu, Y. Liu, *Adv. Mater.* **2018**, *30*, 1801951.
- [3] K. Shi, W. Zhang, D. Gao, S. Zhang, Z. Lin, Y. Zou, L. Wang, G. Yu, *Adv. Mater.* **2018**, *30*, 1705286.
- [4] J. Lee, a. R. Han, J. Kim, Y. Kim, J. H. Oh, C. Yang, *J. Am. Chem. Soc.* **2012**, *134*, 20713.
- [5] G. Dell'Erba, A. Luzio, D. Natali, J. Kim, D. Khim, D. Y. Kim, Y. Y. Noh, M. Caironi, *Appl. Phys. Lett.* **2014**, *104*, 153303.
- [6] C. S. Lao, Q. Kuang, Z. L. Wang, M.-C. Park, Y. Deng, *Appl. Phys. Lett.* **2007**, *90*, 262107.
- [7] J. Wang, H. Wang, X. Yan, H. Huang, D. Jin, J. Shi, Y. Tang, D. Yan, *Adv. Funct. Mater.* **2006**, *16*, 824.

- [8] M. Shkunov, R. Simms, M. Heeney, S. Tierney, I. McCulloch, *Adv. Mater.* **2005**, *17*, 2608.
- [9] Q.-J. Sun, J. Peng, W.-H. Chen, X.-J. She, J. Liu, X. Gao, W.-L. Ma, S.-D. Wang, *Org. Electron.* **2016**, *34*, 118.
- [10] W. Tang, Y. Huang, L. Han, R. Liu, Y. Su, X. Guo, F. Yan, *J. Mater. Chem. C* **2019**, *7*, 790.
- [11] T. Sekitani, U. Zschieschang, H. Klauk, T. Someya, *Nat. Mater.* **2010**, *9*, 1015.
- [12] H. Yoo, M. Ghittorelli, E. C. P. Smits, G. H. Gelinck, H.-K. Lee, F. Torricelli, J.-J. Kim, *Sci. Rep.* **2016**, *6*, 35585.
- [13] J. Zaumseil, H. Sirringhaus, *Chem. Rev.* **2007**, *107*, 1296.
- [14] J. Dong, P. Yu, S. A. Arabi, J. Wang, J. He, C. Jiang, *Nanotechnology* **2016**, *27*, 275202.
- [15] S. Biswas, Y. Yang, C. M. Schlepütz, N. Geva, R. L. Headrick, R. Pindak, R. Clarke, M. Shtein, *Adv. Funct. Mater.* **2014**, *24*, 3907.
- [16] a. Sharma, F. van Oost, M. Kemerink, P. a. Bobbert, *Phys. Rev. B* **2012**, *85*, 1.
- [17] S. Cho, J. Lee, M. Tong, J. H. Seo, C. Yang, *Adv. Funct. Mater.* **2011**, *21*, 1910.

- [18] K. Yamane, H. Yanagi, A. Sawamoto, S. Hotta, *Appl. Phys. Lett.* **2007**, *90*, 2005.
- [19] N. Ahn, K. Kwak, M. S. Jang, H. Yoon, B. Y. Lee, J. K. Lee, P. V. Pikhitsa, J. Byun, M. Choi, *Nat. Commun.* **2016**, *7*, 1.
- [20] S. J. Noever, S. Fischer, B. Nickel, *Adv. Mater.* **2013**, *25*, 2147.
- [21] V. Tamilavan, K. H. Roh, R. Agneeswari, D. Y. Lee, S. Cho, Y. Jin, S. H. Park, M. H. Hyun, *J. Polym. Sci. Part A Polym. Chem.* **2014**, *52*, 3564.
- [22] J. Lee, Y. K. Jung, D. Y. Lee, J.-W. Jang, S. Cho, S. Son, J. Jeong, S. H. Park, *Synth. Met.* **2015**, *199*, 408.
- [23] J. Shi, H. Wang, D. Song, H. Tian, Y. Geng, D. Yan, *Adv. Funct. Mater.* **2007**, *17*, 397.
- [24] V. Tamilavan, Y. Liu, I. Shin, J. Lee, J. H. Jeong, Y. K. Jung, S. H. Park, *J. Photochem. Photobiol. A Chem.* **2019**, *368*, 162.
- [25] X. Song, N. Gasparini, M. M. Nahid, S. H. K. Paleti, C. Li, W. Li, H. Ade, D. Baran, *Adv. Funct. Mater.* **2019**, DOI: 10.1002/adfm.201902441.
- [26] H. Zhang, F. Zhang, J. Sun, M. Zhang, Y. Hu, Z. Lou, Y. Hou, F. Teng, *Appl. Surf. Sci.* **2019**, *478*, 699.

- [27] T. Fukuda, A. Sato, *Org. Electron.* **2015**, 26, 1.
- [28] S. Xie, J. Wang, R. Wang, D. Zhang, H. Zhou, Y. Zhang, D. Zhou, *Chinese Chem. Lett.* **2019**, 30, 217.
- [29] H.-C. Liao, C.-C. Ho, C.-Y. Chang, M.-H. Jao, S. B. Darling, W.-F. Su, *Mater. Today* **2013**, 16, 326.



Chapter 6 Summary and outlook

This dissertation aimed to investigate how improvements could be made to current optoelectronic and electronic devices for the printable displays through the employment of specific functional materials. Two major devices, LEDs and OFETs were studied for improvement in the performance and the functionality. For PeLEDs, a novel conjugated oligoelectrolytes were introduced as a surface passivator result in the CE and maximum luminance increased. PL intensity and film stability are also improved by passivation. For OFETs, a complete bipolar transporting active layer was obtained by employing PBDTTPPD and PCBM. I believe that this study makes a significant contribution to the literature because A-OFETs allow a significant reduction in the complexity of organic integrated circuits. The field of display electronics is advancing fast with improved processing technology of active materials. These new processing techniques offer potential solutions to developing cheap and efficient displays with solution-processing.

Publications

1. Dal Yong Lee, et al. "Solution-processable ambipolar organic field-effect transistors with bilayer transport channels", under revision
2. Dal Yong Lee, Vellaiappillai Tamilavan, Sung Heum Park, and Jong-Kyu Lee. 2017. "Enhancement in the Device Performance of an Organic Field-Effect Transistor Through Thermal Annealing." *New Physics: Sae Mulli* 67 (10): 1180–86.
3. Vellaiappillai Tamilavan, Dal Yong Lee, Rajalingam Agneeswari, Shinuk Cho, Youngeup Jin, Sung Heum Park, and Myung Ho Hyun. 2015. "Tuning the Physical Properties of Pyrrolo[3,4-c]Pyrrole-1,3-Dione-Based Highly Efficient Large Band Gap Polymers via the Chemical Modification on the Polymer Backbone for Polymer Solar Cells." *RSC Advances* 5 (120): 99217–27.
4. Jihoon Lee, Dal Yong Lee, and Sung Heum Park. 2015. "Study of Solution-Processable Bilayer Polymer Solar Cells." *New Physics: Sae Mulli* 65 (8): 741–46.
5. Hoyeon Choi, Vellaiappillai Tamilavan, Dal Yong Lee, Seungmin Kim, Jihoon Lee, Yun Kyung Jung, Seung Hwan Oh, et al. 2016. "Successful Incorporation of

- Optical Spacer and Additive Solvent for Enhancing the Photocurrent of Polymer Solar Cell.” *Solar Energy Materials and Solar Cells* 153 (August): 131–37.
6. Jihoon Lee, Yun Kyung Jung, Dal Yong Lee, Jae Won Jang, Shinuk Cho, Semo Son, Junghyun Jeong, and Sung Heum Park. 2015. “Enhanced Efficiency of Bilayer Polymer Solar Cells by the Solvent Treatment Method.” *Synthetic Metals* 199 (January): 408–12.
 7. Vellaiappillai Tamilavan, Seungmin Kim, Rajalingam Agneeswari, Dal Yong Lee, Shinuk Cho, Junghyun Jeong, Youngeup Jin, Sung Heum Park, and Myung Ho Hyun. 2018. “Two New Tercopolymers Incorporating Electron-Rich Benzodithiophene and Electron-Accepting Pyrrolo[3,4-c]Pyrrole-1,3-Dione and Difluorobenzothiadiazole Derivatives for Polymer Solar Cells.” *Polymer Bulletin* 75 (1): 239–53.
 8. Vellaiappillai Tamilavan, Jihoon Lee, Dal Yong Lee, Rajalingam Agneeswari, Yun Kyung Jung, Youngeup Jin, Jung Hyun Jeong, Myung Ho Hyun, and Sung Heum Park. 2018. “Pyrrole N -Alkyl Side Chain Effects on the Properties of Pyrrolo[3,4- c] Pyrrole-1,3-Dione-Based Polymers for Polymer Solar Cells.” *New Journal of Chemistry* 42 (14): 12045–53.
 9. Yanliang Liu, Insoo Shin, In Wook Hwang, Jihoon Lee, Seungmin Kim, Dal Yong Lee, Seung Hoon Lee, et al. 2017. “Effective Hot-Air Annealing for Improving the Performance of Perovskite Solar Cells.” *Solar Energy* 146 (April): 359–67.

10. Vellaiappillai Tamilavan, Seungmin Kim, Jiyeong Sung, Dal Yong Lee, Shinuk Cho, Youngeup Jin, Junghyun Jeong, Sung Heum Park, and Myung Ho Hyun. 2017. "Enhanced Photovoltaic Performances of Bis(Pyrrolo[3,4-c]Pyrrole-1,3-Dione)-Based Wide Band Gap Polymer via the Incorporation of an Appropriate Spacer Unit between Pyrrolo[3,4-c]Pyrrole-1,3-Dione Units." *Organic Electronics* 42 (March): 34–41.
11. Vellaiappillai Tamilavan, Jihoon Lee, Rajalingam Agneeswari, Dal Yong Lee, Yun Kyung Jung, Shinuk Cho, Jung Hyun Jeong, Youngeup Jin, Myung Ho Hyun, and Sung Heum Park. 2017. "Efficient Pyrrolo[3,4-c]Pyrrole-1,3-Dione-Based Wide Band Gap Polymer for High-Efficiency Binary and Ternary Solar Cells." *Polymer* 125 (September): 182–89.
12. Vellaiappillai Tamilavan, Seungmin Kim, Rajalingam Agneeswari, Dal Yong Lee, Shinuk Cho, Youngeup Jin, Junghyun Jeong, Sung Heum Park, and Myung Ho Hyun. 2016. "Benzodithiophene Based Ternary Copolymer Containing Covalently Bonded Pyrrolo[3,4-c]Pyrrole-1,3-Dione and Benzothiadiazole for Efficient Polymer Solar Cells Utilizing High Energy Sunlight." *Organic Electronics: Physics, Materials, Applications* 38 (November): 283–91.
13. Vellaiappillai Tamilavan, Yanliang Liu, Rajalingam Agneeswari, Dal Yong Lee, Shinuk Cho, Youngeup Jin, Sung Heum Park, and Myung Ho Hyun. 2016. "Property Modulation of Ternary Copolymer via the Diverse Arrangements of

- Two Different Repeating Units for Polymer Solar Cells and Thin Film Transistors.” *Polymer (United Kingdom)* 95: 18–25.
14. Vellaiappillai Tamilavan, Seungmin Kim, Ji Yeong Sung, Dal Yong Lee, Shinuk Cho, Youngeup Jin, Junghyun Jeong, Sung Heum Park, and Myung Ho Hyun. 2016. “Effects of the Incorporation of Bithiophene Instead of Thiophene between the Pyrrolo[3,4-c]Pyrrole-1,3-Dione Units of a Bis(Pyrrolo[3,4-c]Pyrrole-1,3-Dione)-Based Polymer for Polymer Solar Cells.” *New Journal of Chemistry* 40 (12): 10153–60.
15. Juae Kim, Joo Young Shim, Jihoon Lee, Dal Yong Lee, Sangmin Chae, Jinwoo Kim, Il Kim, Hyo Jung Kim, Sung Heum Park, and Hongsuk Suh. 2016. “Syntheses of Pyrimidine-Based Polymers Containing Electron-Withdrawing Substituent with High Open Circuit Voltage and Applications for Polymer Solar Cells.” *Journal of Polymer Science Part A: Polymer Chemistry* 54 (6): 771–84.
16. Rajalingam Agneeswari, Insoo Shin, Vellaiappillai Tamilavan, Dal Yong Lee, Shinuk Cho, Youngeup Jin, Sung Heum Park, and Myung Ho Hyun. 2016. “Effects of the Incorporation of an Additional Pyrrolo[3,4-c]Pyrrole-1,3-Dione Unit on the Repeating Unit of Highly Efficient Large Band Gap Polymers Containing Benzodithiophene and Pyrrolo[3,4-c]Pyrrole-1,3-Dione Derivatives.” *Organic Electronics: Physics, Materials, Applications* 30: 253–64.
17. Juae Kim, Jihoon Lee, Sangmin Chae, Joo Young Shim, Dal Yong Lee, Il Kim,

- Hyo Jung Kim, Sung Heum Park, and Hongsuk Suh. 2016. "Conjugated Polymers Containing Pyrimidine with Electron Withdrawing Substituents for Organic Photovoltaics with High Open-Circuit Voltage." *Polymer (United Kingdom)* 83 (January): 50–58.
18. Rajalingam Agneeswari, Kyung Hwan Roh, Vellaiappillai Tamilavan, Dal Yong Lee, Shinuk Cho, Youngeup Jin, Sung Heum Park, and Myung Ho Hyun. 2015. "Opto-Electrical, Charge Transport and Photovoltaic Property Modulation of 2,5-Di(2-Thienyl)Pyrrole-Based Polymers via the Incorporation of Alkyl, Aryl and Cyano Groups on the Pyrrole Unit." *Polymer Bulletin* 72 (8): 1899–1919.
19. Vellaiappillai Tamilavan, Jihoon Lee, Rajalingam Agneeswari, Dal Yong Lee, Shinuk Cho, Youngeup Jin, Sung Heum Park, and Myung Ho Hyun. 2015. "Photocurrent Enhancement of an Efficient Large Band Gap Polymer Incorporating Benzodithiophene and Weak Electron Accepting Pyrrolo[3,4-c]Pyrrole-1,3-Dione Derivatives via the Insertion of a Strong Electron Accepting Thieno[3,4-b]Thiophene Unit." *Polymer (United Kingdom)* 80 (December): 95–103.
20. Vellaiappillai Tamilavan, Jihoon Lee, Rajalingam Agneeswari, Dal Yong Lee, Shinuk Cho, Youngeup Jin, Sung Heum Park, and Myung Ho Hyun. 2015. "Property Modulation of Dithienosilole-Based Polymers via the Incorporation of Structural Isomers of Imide- and Lactam-Functionalized Pyrrolo[3,4-c]Pyrrole

- Units for Polymer Solar Cells.” *Polymer (United Kingdom)* 65: 243–52.
21. Vellaiappillai Tamilavan, Kyung Hwan Roh, Rajalingam Agneeswari, Dal Yong Lee, Shinuk Cho, Youngeup Jin, Sung Heum Park, and Myung Ho Hyun. 2015. “Benzodithiophene-Based Broad Absorbing Random Copolymers Incorporating Weak and Strong Electron Accepting Imide and Lactam Functionalized Pyrrolo[3,4-c]Pyrrole Derivatives for Polymer Solar Cells.” *Macromolecular Chemistry and Physics* 216 (9): 996–1007.
22. Rajalingam Agneeswari, Insoo Shin, Vellaiappillai Tamilavan, Dal Yong Lee, Shinuk Cho, Youngeup Jin, Sung Heum Park, and Myung Ho Hyun. 2015. “Modulation of the Properties of Pyrrolo[3,4-c]Pyrrole-1,4-Dione Based Polymers Containing 2,5-Di(2-Thienyl)Pyrrole Derivatives with Different Substitutions on the Pyrrole Unit.” *New Journal of Chemistry* 39 (6): 4658–69.
23. Ina Jeong, Juae Kim, Jinwoo Kim, Jihoon Lee, Dal Yong Lee, Il Kim, Sung Heum Park, and Hongsuk Suh. 2016. “6-(2-Thienyl)-4H-Thieno[3,2-b]Indole Based Conjugated Polymers with Low Bandgaps for Organic Solar Cells.” *Synthetic Metals* 213 (March): 25–33.

Acknowledgements

부푼 마음을 안고 부경대학교 물리학과에 입학한 게 바로 얼마 전인 것 같은데 벌써 박사학위를 받는다는 것이 기쁘면서도 어딘가 아쉽습니다. 대학원을 진학하면서도 졸업은 정말 멀고 먼 보이지 않는 임의의 ‘시간 t ’이라고 생각했는데, 벌써 그 시간의 끝에 다다랐다 하니 정말 세월이 쏜살같다는 말이 하나도 틀린 게 없다고 느껴집니다. 그동안 도움을 주신 분들에게, 이젠 제 삶의 대부분을 차지하는 학위과정 동안 쌓여온 고마운 마음을 짧은 지면을 빌려 전합니다.

학부생 시절 저는 반도체와 과학에 관심이 많았고, 그저 더 깊고 더 많은 것을 접할 수 있을 것이라는 생각으로 무작정 박성흠 교수님 연구실 인원 모집에 지원을 했던 것이 생각납니다. 그 시절 물리학에 갖고 있는 관심과는 달리 실제 학업에는 관심과 노력을 기울이지 않았던 저에게 관찰력과 사고력을 높이 평가해 주시며 연구실 입실을 허락해주신 교수님은 제 인생에 큰 전환점이 될 기회를 부여해 주셨습니다. 못난 제자이지만 앞으로 나아갈 수 있도록 끊임없이 독려해 주셨기에, 무사히 학위를 마무리할 수 있었음에 깊이 감사드립니다.

그리고 힘든 시기마다 아낌없이 격려를 해주신 정윤경 교수님께도 감

사드립니다. 또한 바쁘신 와중에도 시간을 내어 박사학위 평가를 맡아 주신 정중현 교수님과 이보람 교수님, 손세모 교수님, 박운익 교수님께 깊은 감사의 말씀을 드립니다. 트랜지스터를 공부할 수 있도록 실험실을 제공해주시고, 교본이 되어주신 조신욱 교수님, 그리고 제가 다양한 신물질들을 공부할 수 있는 기회를 주신 현명호 교수님, 진영읍 교수님, 서홍석 교수님, 이병훈 교수님께 깊이 감사드립니다. 교수님들 한 분 한 분이 쌓아오신 경험과 발자취는 제가 용기를 얻을 수 있는 동력원이었습니다. 발광 다이오드 공부를 시작함에 있어 많은 정보와 도움을 주고, 신물질을 다룰 기회를 주신 박성욱 박사님께도 감사를 드립니다. 함께 연구를 진행하며 많은 신규 고분자를 제작하고 공부할 기회를 나눠준 Tamilavan 박사님과 Agneeswari 박사님, 김주애 박사님에게도 감사를 드립니다.

또한 강산이 변할 만큼 오랜 시간동안 같은 연구실에서 함께 공부하고 서로 도와가며 기쁨과 슬픔을 나눈 우리 연구실 식구들 지훈 형님, 인수 형님, 경환이, 승민이, 호연이, 폐시, 근녕이, 현석이, 단비, 소영이, 은혜, 리양, 차오, 유안, 카이, 동근이에게도 고맙다는 말을 전합니다. 같은 공간은 아니었지만 함께 오랫동안 같은 학과에서 동고동락한 연우 누나, 현미 누나, 지철이, 승훈이, 창목이, 양미, 주현이, 병찬이, 현정이, 병철이, 옥희에게도 같은 마음을 전합니다.

멀리 나와 공부를 하고 있기에, 애기 한번 나누는 것이 연례 행사가 되어버린 친구들 진택이, 윤영이, 태우, 현식이, 승호, 정환이에게도 오랜 시간을 함께 해주어 고맙다는 말을 전합니다. 제가 이 글에 미처 신지 못한 분들에게도 감사의 인사를 전하고 싶습니다.

그리고 무엇보다 제가 여기까지 올 수 있도록 응원과 격려를 아끼지 않으신 아버지, 어머니께는 감사하단 말과 함께 무엇보다 사랑한다는 말을 전하고 싶습니다. 그리고 길고 긴 시간동안 저를 믿어주고 믿어준 너무나도 고마운 아내와 우리 복들이 아들, 그리고 곧 가장 큰 선물이 되어 줄 둘째에게도 사랑한다는 말을 전합니다.

짧지만 결코 가볍지 않은 고마운 마음을 담아 써 내린 이 글이 무색해 지지 않도록 이 후에도 더욱 정진하며 열심히 살겠습니다.

이달용 올림